Fluid-rock reaction path modeling of uranium mobility in granite-related mineralization: A case study from the Variscan South Armorican Domain

Khaled Bock, Yannick Branquet, Olivier Pourret, Philippe Boulvais

Journal Pre-proof

Fluid-rock reaction path modeling of uranium mobility in granite-related mineralization: A case study from the Variscan South Armorican Domain

Khaled Bock, Yannick Branquet, Olivier Pourret, Philippe Boulvais

PII: S0883-2927(24)00346-9

DOI: https://doi.org/10.1016/j.apgeochem.2024.106241

Reference: AG 106241

To appear in: *Applied Geochemistry*

Received Date: 18 July 2024

Revised Date: 21 November 2024

Accepted Date: 26 November 2024

Please cite this article as: Bock, K., Branquet, Y., Pourret, O., Boulvais, P., Fluid-rock reaction path modeling of uranium mobility in granite-related mineralization: A case study from the Variscan South Armorican Domain, *Applied Geochemistry*, https://doi.org/10.1016/j.apgeochem.2024.106241.

Fluid-rock reaction path modeling of uranium mobility in granite-related mineralization: A case study from the Variscan South Armorican Domain

Khaled Bock[1], Yannick Branquet[1], Olivier Pourret[2], Philippe Boulvais[1]

[1] *Univ Rennes, CNRS, Géosciences Rennes, UMR 6118, 35000 Rennes, France*

[2] *UniLaSalle, AGHYLE, 19 rue Pierre Waguet, 60000 Beauvais, France*

Abstract

The mobilization of uranium in granite-related systems presents a complex interplay of chemical and hydrodynamic factors. This is particularly obvious within syn-orogenic detachment zones where *per descensum* surface-derived fluids interact with *per ascensum* deeply sourced hydrothermal fluids. In this study, we employ a thermo-hydro-chemical (TH-C) modeling approach to explore the multifaceted processes that govern uranium transport and deposition in such environments. Our findings indicate that uranium mobility is not solely determined by the oxidizing nature of the percolating surface-derived fluids. Actually, the oxidation-reduction potential of these fluids varies as they flow in the crust, ultimately adjusting towards more neutral or mildly reducing conditions conducive to uranium dissolution and precipitation. Even in the presence of magnetite, which enhances the reductive potential of the fluids, uranium continues to dissolve, albeit in much smaller quantities, with U(IV) being the predominant species in the aqueous phase. The study highlights the crucial roles of temperature, pH, and fluid/rock interaction ratios in influencing uranium leaching efficacy. High fluid/rock ratios enhance uranium extraction from source rocks. A fluid/rock ratio around 1 is optimal, maximizing the dissolution of uranium-bearing minerals in the source rock and promoting the precipitation of uranium minerals in different locations along the fluid pathway due to changes in fluid chemistry. The TH-C modeling has the potential to be applied to a variety of other uranium deposits, developed below 300°C.

Key-words: Uranium Mobilization; Fluid/Rock Interaction; Redox Potential; Thermo-Hydro-Chemical Modeling (TH-C); Syn-kinematic Granite; Detachment Zones.

1. Introduction

Uranium mineralization associated with granites emerges as an important category among the various types of uranium deposits, demonstrating widespread occurrences worldwide (Cuney, 2009, 2010; Romer and Cuney, 2018). These deposits account for 29% of the total identified uranium resources in China (Woods et al., 2019). The Variscan belt hosts numerous uranium deposits that are both spatially and temporally associated with granites (Cuney et al., 1990; Marignac and Cuney, 1999; Kříbek et al., 2009; René and Dolníček, 2017; Romer and Cuney, 2018; Mikulski et al., 2020), especially with peraluminous syn-kinematic granites (Poty et al., 1986; Cathelineau et al., 1990; Cuney et al., 1990; Tartèse et al., 2013; Ballouard et al., 2017).

The interplay between hydrothermal fluids circulations and the activity of shear zones, particularly in the context of syn-kinematic granite emplacement helps understanding the genesis of uranium deposits. Advances in this area are propelled by geological characterization, which allows building conceptual models (e.g., Ballouard et al., 2017; Qiu et al., 2018). Besides, numerical studies have been developed to reconstruct the physical conditions under which hydrothermal circulations in permeable zones have enabled the development of comprehensive thermo-hydrodynamic models (e.g., Eldursi et al., 2009; Souche et al., 2014; Labrousse et al., 2016; Bock et al., 2024). Despite these advances, current fully-coupled numerical studies (i.e., Thermo-Hydro-Mechanical-Chemical, THMC) have not yet reached the level of sophistication required to encompass the bulk complexities, among which are chemical aspects associated with hydrothermal circulation especially linked to granite emplacement.

At high temperatures, from 300°C to magmatic conditions (~650°C), the chemical processes involved in uranium mobilization and trapping are underexplored (Cuney and Kyser, 2009). This is primarily due to the limitations of current thermodynamic databases, which only cover uranium species up to a maximum temperature of 300°C (Pearson and Berner, 1991). Below 300°C, the understanding of uranium geochemistry is sufficient to model the mechanisms of uranium dissolution and precipitation (Romberger 1984; Timofeev et al., 2018). The oxidation state of uranium is a critical factor in determining its geochemical behavior. Under reducing conditions, tetravalent uranium (U(IV)) commonly forms poorly soluble phases, thereby limiting its mobility in aqueous fluids, whereas hexavalent uranium (U(VI)) is significantly more soluble, enhancing its transport (Langmuir, 1997; Grenthe et al., 1992; Finch and Ewing, 1992; Curtis et al., 2006; Cuney and Kyser, 2009; Spycher et al., 2011). This underscores the importance of redox conditions and ligand complexation in controlling uranium behavior in geological environments (Langmuir, 1978; Abdelouas, 2006). However, it is also recognized that uranium can sometimes remain mobile under reducing conditions, particularly when complexed with ligands such as chloride. Recent experimental investigations by Timofeev et al. (2018) have identified a novel uranium chloride species, $UCl_4°$, that demonstrates greater thermodynamic stability under reducing conditions compared to oxidizing conditions. Furthermore, the mobility of uranium is influenced by the solubility of its complexes, with predictions of uranium migration being inherently complex due to the interplay between temperature gradients, pH variations and changes in oxidation states (Carnahan, 1986).

Addressing the metallogenic triptych of source, transport and deposition necessitates tracking fluid-rock interactions across various temperature fields and fluid/rock ratios. This complexity has not been thoroughly characterized for uranium, particularly regarding chemical conditions such as redox potential, pH and speciation (White, 1968). To bridge this gap, we have developed a TH-C modeling approach, complementary to methods such as thermo-hydro-

chemical coupling (THCC) employed by Carnahan (1986). The TH-C approach investigates uranium mobility in relation to fluid flow associated with granitic intrusions in tectonically active settings dominated by detachment faulting. This local uranium mobility can lead to uranium mineralization, as seen in the Variscan South Armorican uranium system (Ballouard et al., 2017), which serves as an application of our modeling. The aim of this study is to enhance our understanding of uranium speciation, redox conditions and of the interactions between uranium-bearing fluids and host rocks, especially in cases where fluids encounter relatively high temperature conditions (around 300°C).

2. The Variscan South Armorican Domain as a case study

Uranium deposits associated with peraluminous granites are found worldwide, for instance and among numerous others, in the Erzgebirge-Krušné Hory region spanning Germany and the Czech Republic (Zhang et al., 2017) and in the Motianling uranium district of South China (Qiu et al., 2018). The South Armorican Massif uranium deposits investigated in this study (Fig. 1) exemplify a general case study of granite-related uranium deposits (e.g., Cuney, 1978; Tartèse et al., 2013; Ballouard et al., 2017).

In the southern region of the Armorican Massif (Fig. 1a), the Guérande leucogranite was emplaced around 300 Ma along a late-orogenic detachment fault (Ballouard et al., 2015). It hosts a cluster of uranium deposits (Fig. 1b). The uranium mineralization has been dated between 300 and 275Ma (Ballouard et al., 2017). It coincides with late intrusion of microgranite dykes around 300 Ma and on-going hydrothermal pulses. Some uranium deposits occur at the faulted contact between black shales and metavolcanics, commonly known as porphyroids (see Fig. 1c and 1d), which are situated over the apical zone of the intrusion (see Fig. 1e and f). Primary enrichment in uranium in this apical zone is basically a consequence of

98 fractional crystallization which led to uraninite crystallization in the main granitic pluton
99 (Ballouard et al., 2017).

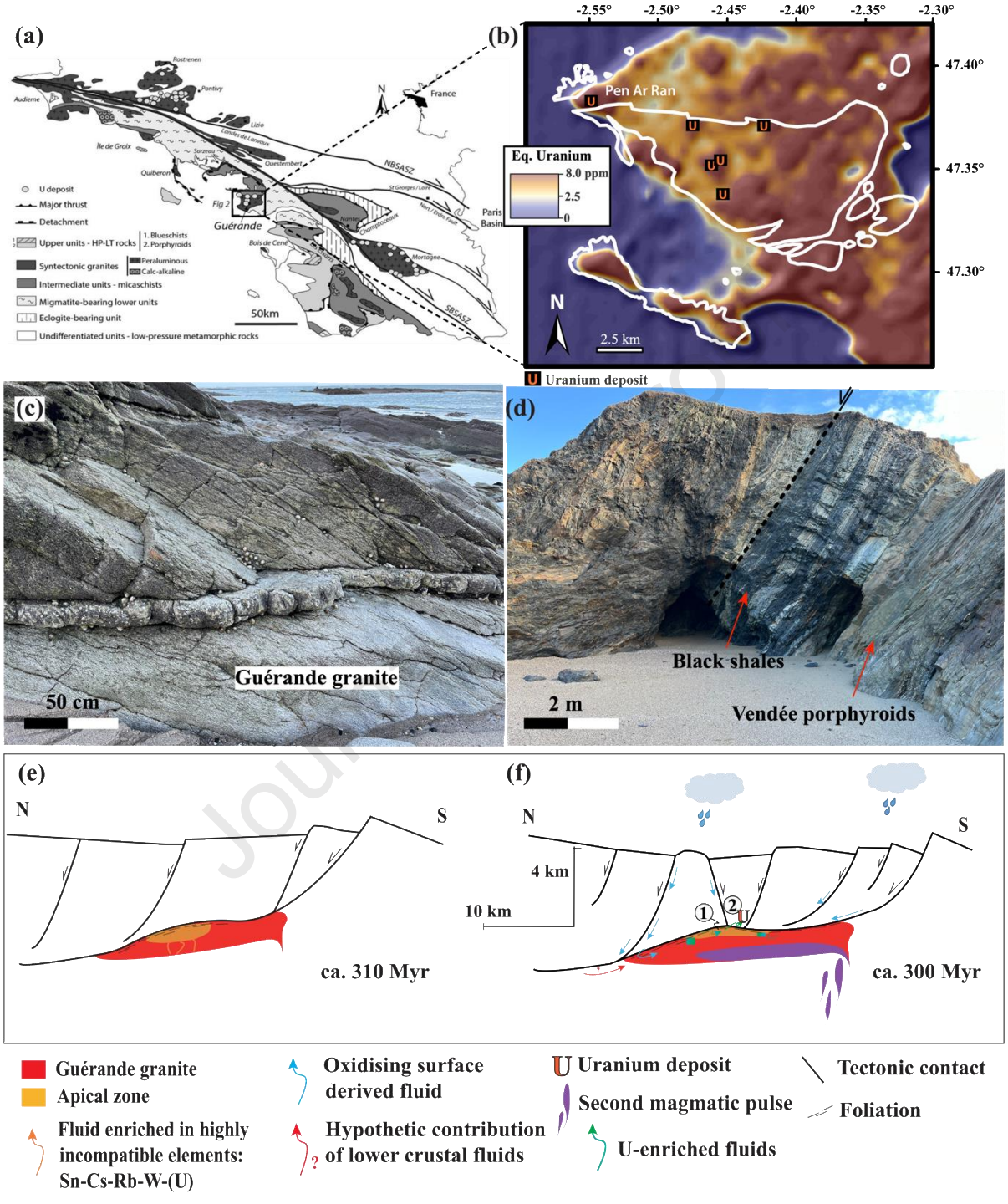

100

101 Figure 1: (a): Simplified geological map of the South American Domain; the insert corresponds to the Variscan
102 Guérande pluton (Ballouard et al., 2017)). (b): Airborne radiometric map showing the distribution of uranium
103 deposits in the Guérande area. The white line corresponds to the cartographic contour of the Guérande pluton
104 (Ballouard et al., 2017). (c) and (d) are field views, localized in (f), showing respectively the deformed U-rich

apical zone of the leucogranite pluton intersected by a quartz vein (1), and the alternating layers of porphyroids (metavolcanics) and black shales crosscut by a normal fault (2); The Pen Ar Ran uraninite deposit occurs along this fault and was mined about 50 m below the sand beach. (e) and (f) are synthetic cross-sections illustrating the Guérande metallogenic model (Ballouard et al., 2017).

Data from airborne radiometric surveys combined with stable isotopes and fluid inclusions analyses point to the significant leaching of uranium. This leaching was linked to the alteration of uraninite-bearing apical rocks by oxidizing surface-derived fluids (Ballouard et al., 2017). Both the enhanced thermal conditions related to magmatic intrusions, especially during the second magmatic pulse at ca. 300 Ma and the brittle deformation in the hanging wall of the detachment greatly contributed to trigger and maintain fluid circulation and thus mobilization and deposition of uranium.

3. **Modeling background**

Among the various methodologies available for modeling the formation of uranium deposits (e.g., IAEA, 2020; Qu et al., 2021; Shen, 2021), process-based modeling stands out due to its comprehensive approach (Komninou and Sverjensky, 1996). This technique simulates the fundamental geological processes responsible for ore deposits through THMC (Thermo-Hydro-Mechanical-Chemical) modeling, integrating fluid flow, heat transfer, mechanical dynamics and chemical reactions (e.g., Oliver et al., 2006; Harcouët-Menou et al., 2009; Eldursi et al., 2018).

Expanding on the foundation of process-based modeling, reactive transport modeling serves as a critical tool. It couples fluid flow, heat transfer and multicomponent reactive transport equations, demonstrating its robustness in controlled environments such as in situ uranium leaching, as evidenced in studies by Collet et al. (2022), Qiu et al. (2023) and Zhang et al. (2023). The applicability of this method extends to other deposit types, including unconformity-related deposits (e.g., Wang and Chi, 2023). Despite its proven utility, deploying

process-based modeling in large-scale reservoirs spanning tens of kilometers, particularly those subject to multiple driving forces like buoyancy and topography, with high temperatures associated with magma emplacement, poses significant challenges. Solving the thermo-hydrodynamic model in these large dynamic systems leads to considerable computation times and difficulties in achieving model convergence. Additionally, integrating reaction rates between fluids and minerals is challenging due to the lack of data for high-temperature conditions and the complexity of solving numerous reactions simultaneously with temperature and fluid pressure calculations.

Significant progress has been made in large-scale Darcyan hydrothermal system modeling, particularly in coupling heat, multiphase fluid and salinities (Weis et al., 2014). Building on this progress, we have adopted here a commonly used procedure that decouples heat and fluid transport from chemical species reactions. This approach referred to here as TH-C (Thermo-Hydrodynamic-Chemical modeling), allows tackling each component with great focus and specificity, enhancing the accuracy and efficiency of modeling. By solving both thermal and fluid flow processes simultaneously, we can model the influence of heat on fluid flows, including convective heat transport. The way temperature gradients affect fluid circulation can also be targeted. This simultaneous modeling is critical as heat and fluid dynamics are deeply interrelated, and any change in one has a direct impact on the other. For instance, fluid circulation can transport heat through the system, whereas changes in temperature can alter fluid properties such as density and viscosity, which in turn affect flow rates and directions.

Chemical reactions, on the other hand, are resolved separately from the thermal and hydrodynamic processes. This decoupling enables more focused and detailed treatment of chemical interactions, such as mineral dissolution, precipitation and complexation reactions, without the additional computational complexity associated with continuously updating thermal and fluid variables.

4. Strategy and model set-up

4.1 Numerical approach

Bock et al. (2024) solved the equations of heat and fluid transports in uranium-bearing systems associated with detachment and syn-kinematic granites, with an application to the Guérande uranium mineralized system. During periods of plutonic activity, significant downward meteoric fluid flow occurs (Fig. 2a), eventually reaching the apical zone of the granitic pluton. This hydrothermal activity is driven by magmatic emplacement, which increases the buoyancy of the overall system, reinforcing the pre-existing convective flow typically driven by pressure gradients due to surface topography, large permeability contrasts, or both. The influx of thermal energy from the magmatic intrusion promotes the downward movement of surface-derived fluids, which then penetrate deep into the system, eventually reaching the apical zone of the pluton. As these fluids are heated, their density decreases, triggering their upwelling which completes the convective cycle. The pressure-temperature (PT) trajectories of the fluid particles indicate that they remain in the liquid state (Fig. 2b). In the present study, the PT trajectories in space are utilized in an iterative chemical modeling process (Fig. 3). The PHREEQC software (Parkhurst and Appelo 1999) is employed to simulate the interaction of meteoric fluids with rocks at several PT points in three successively infiltrated reservoirs (points 1 to 9; Figs. 3 and 4). This choice of three reservoirs is based on the case of the South American Domain (Fig. 1). Firstly, the fluids flow through the crust (Reservoir 1, points 1 to 4), where it interacts with crustal rocks before reaching the apical zone of the leucogranitic pluton (Reservoir 2, points 5 to 7), the main source of uranium. Then, the fluid leaves the apical domain and enters the black shale reservoir (Reservoir 3, point 8). Return in the crustal first reservoir corresponds to point 9.

PHREEQC is primarily designed for equilibrium chemistry modeling of aqueous solutions as they interact with minerals, gases, solid solutions, exchangers and sorption surfaces. It also has the capability to model kinetic reactions. However, the efficiency of these kinetic models depends on the quality and availability of kinetic data. Given the notable deficiency in kinetic data for uranium species at high temperatures, we have opted for a forward modeling approach based on equilibrium calculations, similar to the approach used by Post et al. (2017). This approach leverages well-established and widely available thermodynamic data, such as solubility constants and Gibbs free energy, applicable to a broad spectrum of minerals and environmental conditions. Notably, our approach incorporates both reduced and oxidized uranium species, providing a comprehensive analysis of uranium mobility under various redox conditions. In our methodology, the output from a calculation at one point provides the basis for the subsequent calculation at the next point. For instance, the fluid composition calculated after the reaction at point 1 is used as the invading fluid for point 2. This procedure continues across the nine modeled batch reactions, with evolving temperatures from 25°C to 300°C (for points 1 to 7) and then from 300°C to 200°C (for points 7 to 9), as shown in Figure 3.

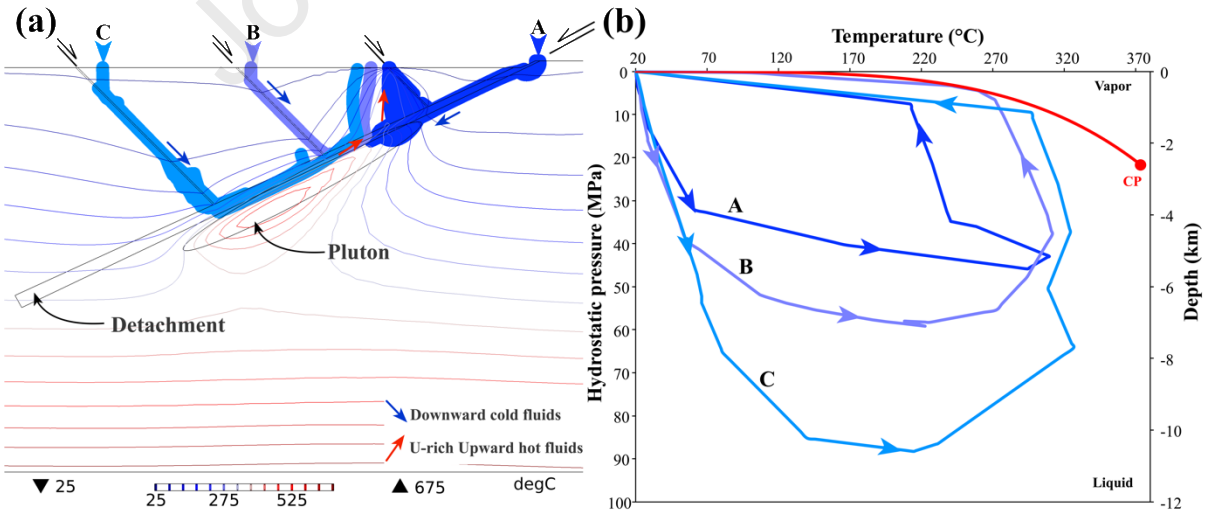

Figure 2: (a) Model of surface-derived fluids infiltration into a detachment zone associated with a syn-kinematic leucogranite pluton (particle tracing from Thermo-hydrodynamic models of Bock et al., 2024). The colored lines

correspond to isotherms. (b) Pressure-temperature diagram where the flow of fluid particles along paths A, B and C are reported (adapted from Bock et al.,2024). CP = Critical Point for pure water (374°C, 22 MPa).

4.2 Experimentation and Sensitivity Studies on Uranium Mobility

The numerical analyses conducted in this study are categorized into three groups:

1. The first group of experiments, referred to as the base model, involves batch reaction computations for the nine designated points (Fig. 3). This setup features a fluid/rock ratio (F/R) of 0.01, with 1 kg of water interacting with 99 kg of rocks.
2. The second experiments undertake a sensitivity analysis to explore the effect of varying fluid/rock ratios on uranium mobility, with F/R of 0.01 (the base model), 0.1, 0.3, 0.5, 0.7, 0.9, 1, 3 and 100.
3. The third experiments focus on a sensitivity analysis concerning the redox conditions of surface-derived fluids. This is conducted for the base model by adding magnetite at two concentrations in Reservoir 1 (0.5 wt.% and 1.6 wt.%; Fig. 4).

4.3 Initial conditions

The initial composition of the meteoric fluid is based on data from Freeze and Cherry (1979). We used the average composition of seven different rain and snow sites across the United States, Australia and Northern Europe, following the approach used by Lee et al. (2003). We set a temperature of 25°C and a typical electron activity (pe) of 11 (Willey et al., 2012) as an input for point 1 (Fig. 3).

Table 1: Rainwater composition and parameters used at the first batch reaction point, with the composition in mg/L and the temperature in degrees Celsius. (Freeze and Cherry, 1979)

Temperature	pH	pe*	Na	K	Ca	Mg	HCO3	SO4	Cl	NO3

25	5.5	11	0.6	0.4	0.9	0.22	2	3	0.4	0.3

219 * Rainwater negative logarithm electrons activity (Willey et al., 2012)

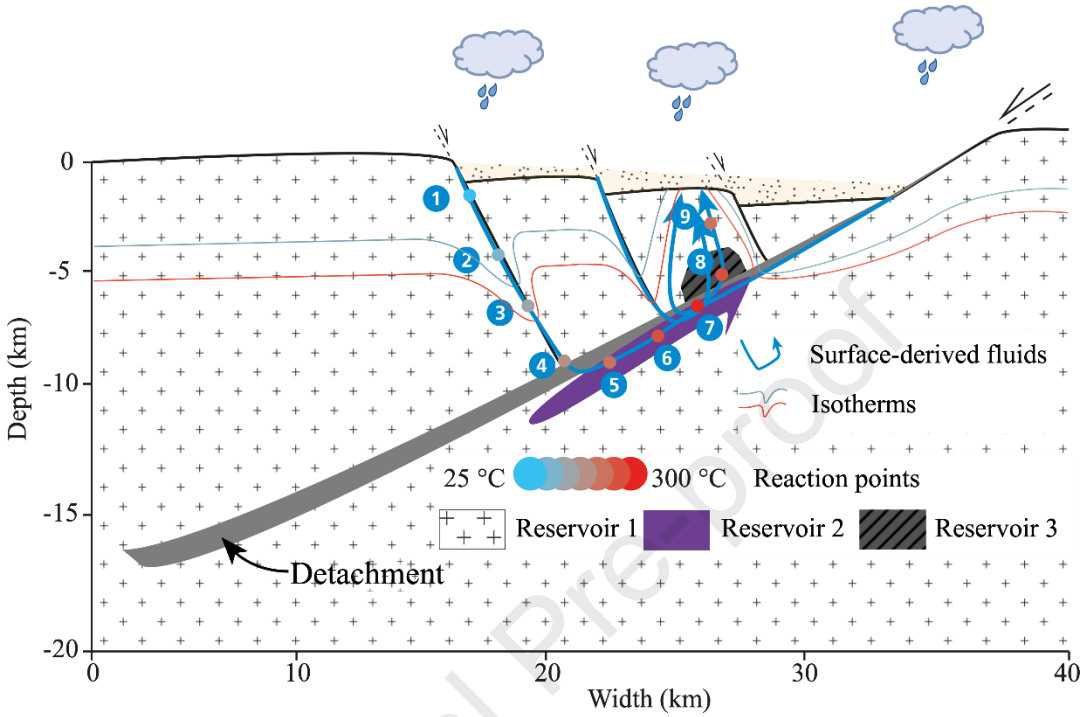

220

221 Figure 3 : Model of meteoric fluid percolation through different geological reservoirs associated with a detachment
222 zone (inspired from the hydro-thermodynamic models of Bock et al., 2024). The location of the 9 reaction points
223 is deduced from particle tracing in Bock et al. (2024) (see also Fig. 2) and is indicated along the flow path of
224 surface-derived fluids (numbered blue circles).

225 Our approach considers the progression of the surface-derived fluids through three geological
226 reservoirs (Fig. 3 and 4). Reservoir 1 is defined using the average composition of the upper
227 continental crust (Taylor and McLennan,1985), with a uranium concentration of 2.8 ppm. In
228 the upper crust, uranium typically occurs as a trace element, often found in minerals like zircon
229 and apatite. However, since these minerals do not have uranium in their chemical formulas, it
230 is difficult to accurately represent uranium in the mineral assemblage for this reservoir.
231 Although we could use a uranium mineral like uraninite to model its presence, this would not
232 accurately reflect how uranium is naturally distributed in the upper crust. For this reason, we
233 have avoided including uranium in the first reservoir composition. Reservoir 2 features a

234 classical leucogranite mineral composition (Harris and Inger, 1992) close to the differentiated
235 facies of the Guérande granite (Ballouard et al., 2015, Fig. 4). In Ballouard et al. (2017), the
236 initial uranium content in the granites is reported as 20 ppm, based on drill core samples from
237 Ouddou (1984). Of this, it is estimated that 50% of the uranium is hosted by uranium oxides.
238 Given that uranium in trace amounts (for the remaining 50%) cannot be accurately modeled
239 due to technical reasons (as previously discussed), we chose to represent only the uranium
240 hosted by uranium oxides. This choice is supported by Ballouard et al. (2017), which argue
241 that uraninite crystallizes in differentiated melts when the uranium content reaches around 10
242 ppm. Based on this information, we selected a uranium concentration of 12.5 mg/kg
243 (corresponding to 0.0014 wt.% of uraninite, Fig. 4) that aligns with the conditions under which
244 uraninite is expected to form. Reservoir 3 is close to Reservoir 1 but it contains pyrite to reflect
245 the reducing property of the black shales where U deposits formed (Fig. 1d and f).

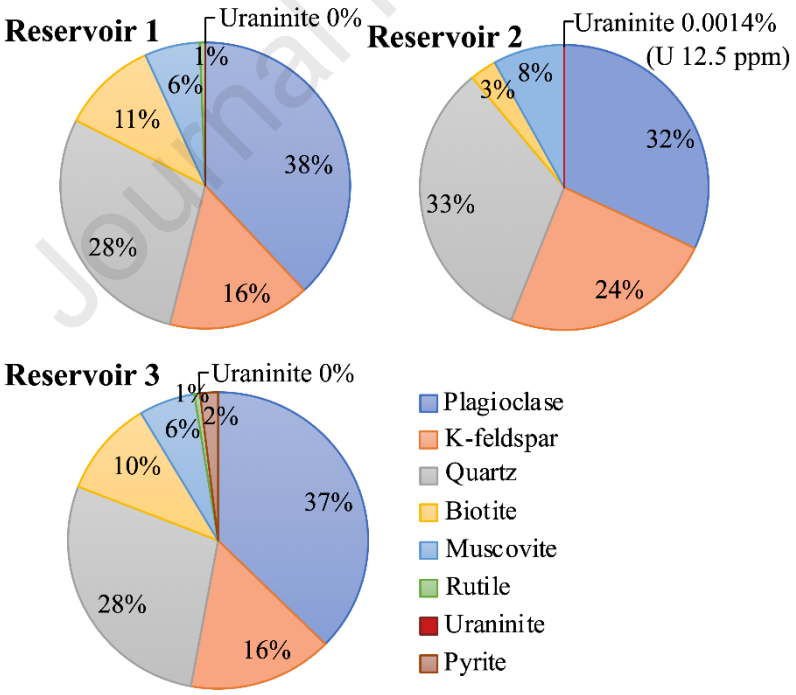

Figure 4: Mineralogical composition in wt.% of the three reservoirs infiltrated by surface-derived fluids. Details and references of the three reservoir compositions are presented in section 4.4.

4.4 Benchmarking

In the preliminary phase of our research, we have conducted a benchmark study using PHREEQC to replicate the uranium speciation model at ambient conditions of 25°C (Fig. 3), as proposed by Tripathi (1979). This benchmarking served as a foundational step in selecting the most appropriate thermodynamic database from those available within PHREEQC. The Lawrence Livermore National Laboratory (LLNL) database emerged as the preferred choice due to its robustness, relevance to our study and comprehensive temperature applicability, supporting simulations up to 300°C. Additionally, it includes an extensive catalog of 2590 species ensuring broad coverage of potential reaction pathways. Crucially, the LLNL database demonstrated high fidelity in mirroring the speciation trends outlined in the model of Tripathi (1979), as shown in Figures 5a and 5b, affirming its utility for our geochemical modeling. This aligns with the compilation of Cuney and Kyser (2009). In Figure 5c, we present the proportions of Ca-U complexes ($CaUO_2(CO_3)_3^{2-}$ and $Ca_2UO_2(CO_3)_3(aq)$) within uranium(VI), which were not identified at the time of the Tripathi calculations.

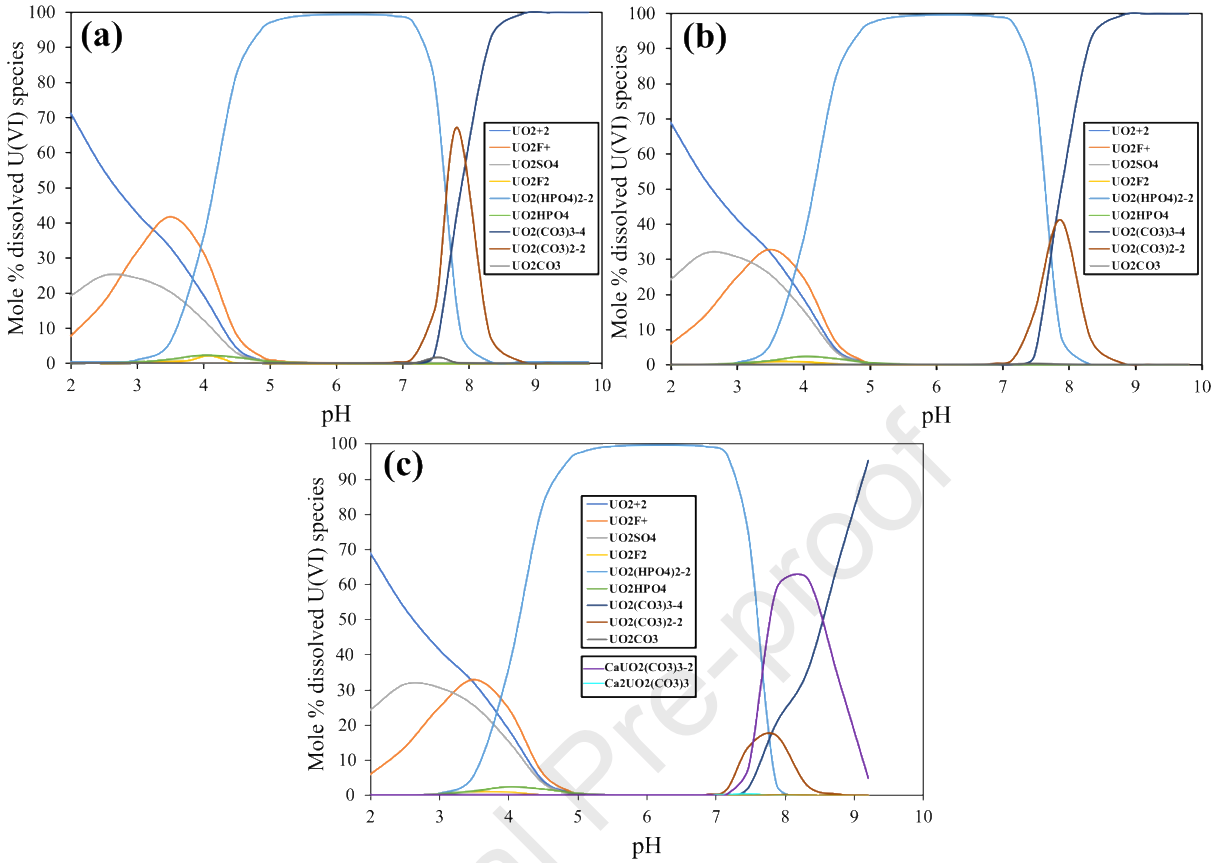

Figure 5: (a) Molar percentage of dissolved uranium (VI) species as a function of pH at 25°C redrawn from Tripathi (1979). Conditions are: $\Sigma U(VI) = 10^{-8}$ M, ΣF = 0.3 ppm, ΣCI = 10 ppm, ΣSO4 = 100 ppm, ΣPO4 = 0.1 ppm, ΣSiO_2 = 30 ppm and $P_{CO2} = 10^{-2.5}$ atm. (b) Our replication of Tripathi (1979) model using the Lawrence Livermore National Laboratory (LLNL) database. (c) Same as (b), but adjusted with Ca = 0.9 ppm to include the percentages of Ca-U complexes that were unknown during the original Tripathi (1979) study.

5. Results

5.1 The base model (Fluid/Rock ratio = 0.01)

5.1.1 Mineral reactions and evolution of pe and pH

The infiltration of fluid through Reservoir 1 is accompanied by an increase in temperature from 25°C to 150°C (points 1 to 4; Fig. 6), a gradual increase in pe and a decrease in pH. From points 1 to 4, there is no U in the solution. The concentrations of Si, Al and K increase, and those of Ca and Mg decrease.

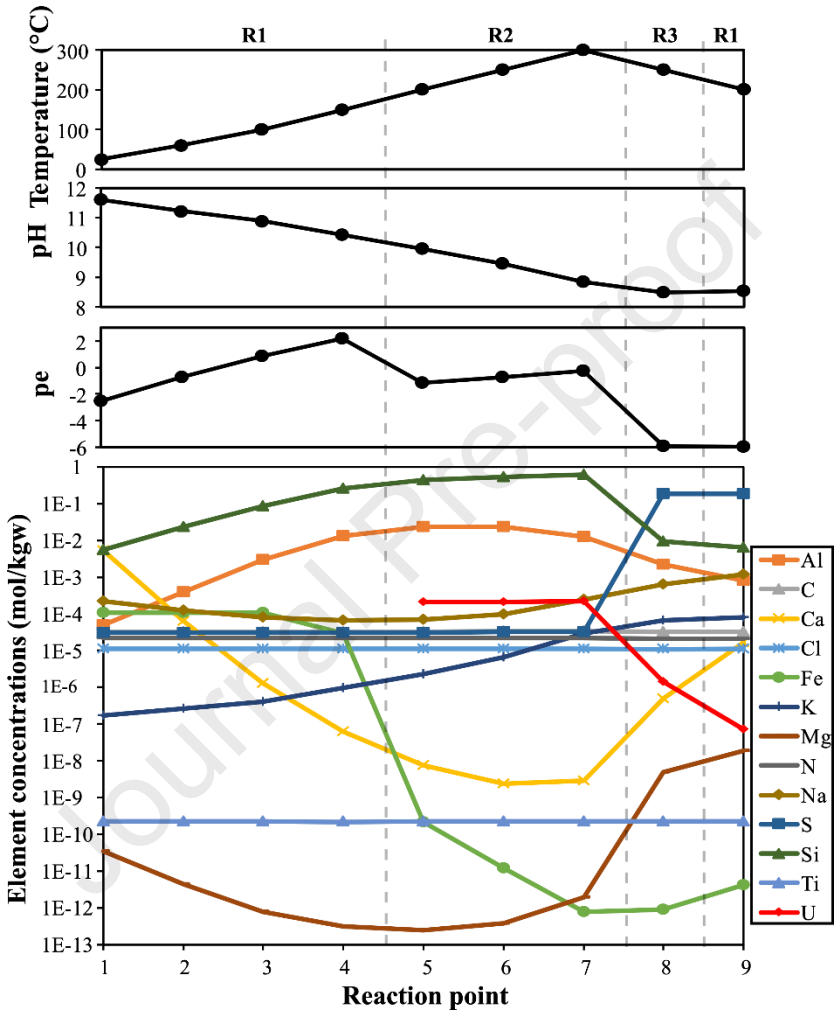

Figure 6: Temperature, pH, pe and concentrations of a variety of elements in the fluid phase for the base model along the flow path represented by the 9 reactions points. The three reservoirs are labeled R1, R2 and R3.

In Reservoir 2, temperature increases from 200°C to 300°C (points 5 to 7) and pH continues to decrease. Concurrently, there is a marked pe drop before a re-increase toward point 7. Dissolution of uraninite is evidenced by the appearance of U in solution (red line in Figure 6). A significant drop in Fe concentration at point 5 then a decrease toward point 7 is observed (Fig. 6).

Upon entering Reservoir 3, the temperature decreases after its peak in Reservoir 2, accompanied by continued pH acidification and a drop in pe. The significant decrease in U concentration indicates precipitation of uraninite. There is also a decrease in the concentrations of Si and Al, and a strong increase in S, Ca and Mg. As the fluid returns to Reservoir 1 at 200°C (point 9), both pe and pH do not vary. The U concentration in the solution drops further, whereas there is a significant increase in the concentrations of Ca, Mg and Fe.

Figure 7 exhibits the variations of mineral content at the equilibrium across the three reservoirs. A negative delta value means that the mineral undergoes dissolution, and a positive delta value means that the mineral undergoes precipitation. These processes of dissolution and precipitation align with the elemental changes in the solution (Fig. 6), providing insight into the fluctuations in pH ($-\log[H^+]$) and pe ($-\log[e^-]$) across the three reservoirs. For instance, the concentration of Fe in Reservoir 1 remains relatively stable (Fig. 6), as annite dissolution at point 1 (Fig. 7) is followed by stabilization. Upon entering Reservoir 2, a marked drop in Fe concentration (Fig. 6) is observed, consistently with the precipitation of annite (Fig. 7). In Reservoir 3, Fe levels increase slightly at points 8 and 9 (Fig. 6), which can be attributed to pyrite dissolution (Fig. 7). This evolution of Fe throughout the system is a key factor in the variations in pe. The rise in pe from -2.5 to 2.2 in Reservoir 1 is primarily driven by the oxidation of ferrous iron (Fe^{2+}) released during the initial dissolution of annite at point 1 (Fig. 7):

$$KFe_3AlSi_3O_{10}(OH)_2 + 10H^+ \rightarrow K^+ + Al^{3+} + 3Fe^{2+} + 3SiO_2 + 6H_2O \quad (1)$$

$$Fe^{2+} \rightarrow Fe^{3+} + e^- \quad (2)$$

Although annite undergoes precipitation in subsequent points of Reservoir 1, the moles of Fe^{2+} released from its initial dissolution exceed the amount removed through precipitation. This

surplus of Fe^{2+} in the aqueous phase sustains oxidation reactions, consuming electrons and driving the increase in pe (Reaction 2).

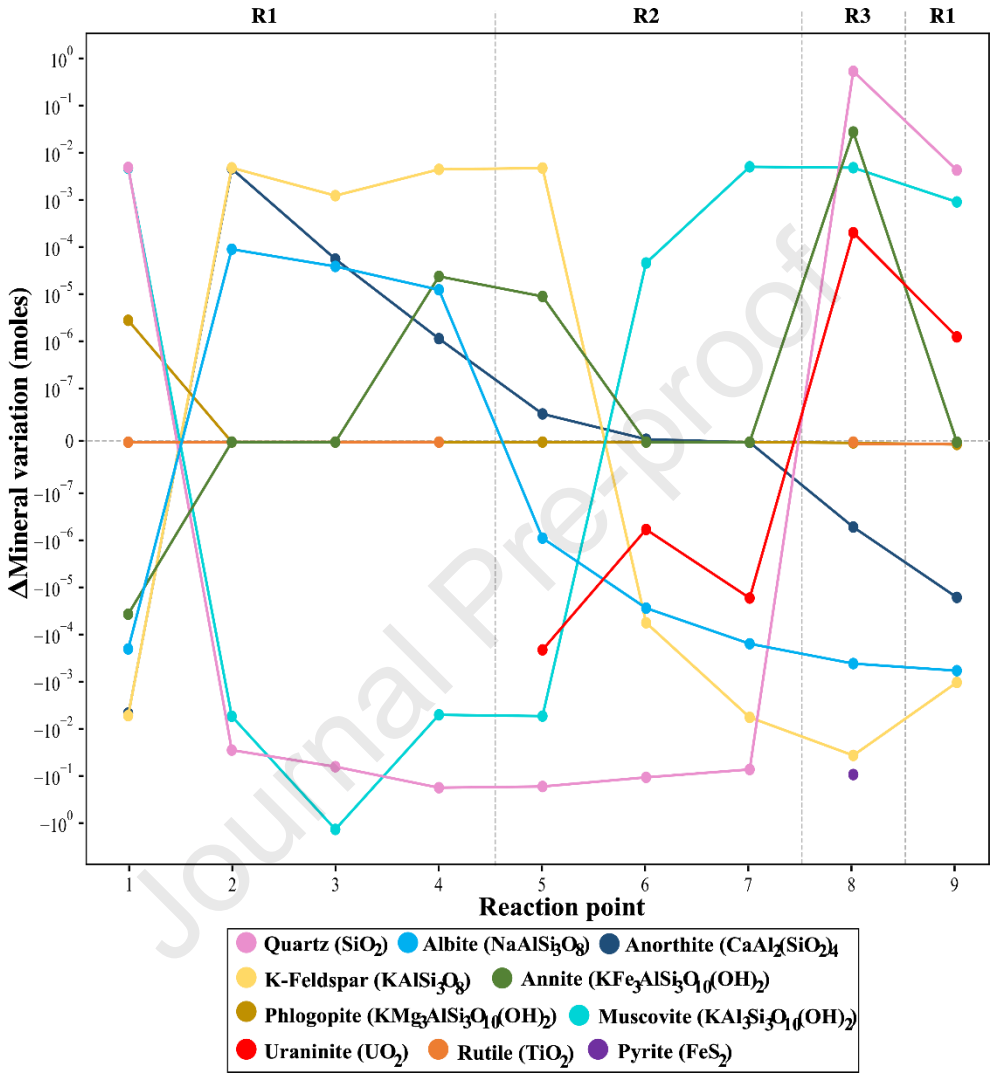

Figure 7: Variation in mineral concentrations (in moles) within the rock across the nine reaction points, plotted on a symmetric logarithmic scale. Rutile is absent in Reservoir 2, and pyrite is present only in Reservoir 3 (see Fig. 4 for details).

The sudden drop in pe from 2.2 to -1.1, at the transition to Reservoir 2 (Fig. 6), is primarily driven by the dissolution and oxidation of uraninite:

$$UO_2 + 4H^+ \rightarrow U^{4+} + 2H_2O \quad (3)$$

Under oxidizing conditions, U^{4+} is readily oxidized to U(VI) in the form of UO_2^{2+}:

$$U^{4+} + 2H_2O \rightarrow UO_2^{2+} + 4H^+ + 2e^- \quad (4)$$

311 Following this sharp drop in pe, a slight increase from -1.1 to -0.27 (Fig. 6) occurs due to the
312 ongoing consumption of electrons remaining in the system (Reaction 2).

313 In Reservoir 3 (point 8), the fluid exhibits a drop in pe to -5.9 (Fig. 6). This significant shift in
314 the redox potential is directly associated with the introduction and dissolution of pyrite (Fig.
315 7):

$$FeS_2 + H_2O \rightarrow 0.25H^+ + 0.25SO_4^{2-} + Fe^{2+} + 1.75HS^- \quad (5)$$

316 During this process, both ferrous iron (Fe^{2+}) and hydrosulfide ions (HS^-) are released, both of
317 which can participate in redox reactions. One key reaction is the oxidation of hydrosulfide
318 (HS^-) to sulfate (SO_4^{2-}), which releases electrons. This increase in electron activity lowers the
319 pe of the system:

$$HS^- + 4H_2O \rightarrow SO_4^{2-} + 9H^+ + 8e^- \quad (6)$$

320 At Point 9 (Reservoir 1), the pe remains relatively constant with only a minor increase from -
321 5.92 to -5.97 as the system is already under strongly reducing conditions due to previous
322 processes, such as pyrite dissolution. The electron consumption from uraninite precipitation is
323 balanced by the limited availability of oxidizing agents, resulting in the pe stabilizing rather
324 than increasing.

325 In terms of pH, the fluid shows a steady decrease from 11.6 at point 1 to 8.4 at point 8, followed
326 by a slight rise to 8.5 at point 9 (Fig. 6). The gradual decline in pH from point 1 to point 8 can
327 be primarily attributed to proton-releasing precipitation reactions, which outweigh proton-
328 consuming dissolution reactions. The precipitation of silicate minerals (Fig. 7), such as annite

329 (Reaction 1), albite (Reaction 7), K-feldspar (Reaction 8), anorthite (Reaction 9), and
330 muscovite (Reaction 10), releases protons (H^+), contributing to an increase in hydrogen ion
331 concentration, thereby lowering the pH:

$$Al^{3+} + Na^+ + 2H_2O + 3SiO_2 \rightarrow NaAlSi_3O_8 + 4H^+ \quad (7)$$

$$K^+ + Al^{3+} + 3SiO_2 + 2H_2O \rightarrow KAlSi_3O_8 + 4H^+ \quad (8)$$

$$Ca^{2+} + 2Al^{3+} + 2SiO_2 + 4H_2O \rightarrow CaAl_2Si_2O_8 + 8H^+ \quad (9)$$

$$K^+ + 3Al_3^+ + 3SiO_2 + 6H_2O \rightarrow KAl_3Si_3O_{10}(OH)_2 + 10H^+ \quad (10)$$

332 In contrast, the subtle rise in pH is primarily due to the dissolution of silicate minerals (Fig. 7).
333 The dissolution of these minerals consumes hydrogen ions, thereby reducing the acidity of the
334 fluid and causing a slight increase in pH at point 9 (Fig. 6).

335 5.1.2 **Uranium solubility and speciation**

336 In Figure 8, we observe an inverse relationship between the U concentration in the solution and
337 the changes in the amount of uraninite in the rock ($\Delta_{Uraninite}$). When U concentration in solution
338 increases, the amount of uraninite decreases due to dissolution, and when U concentration
339 decreases, it increases due to precipitation.

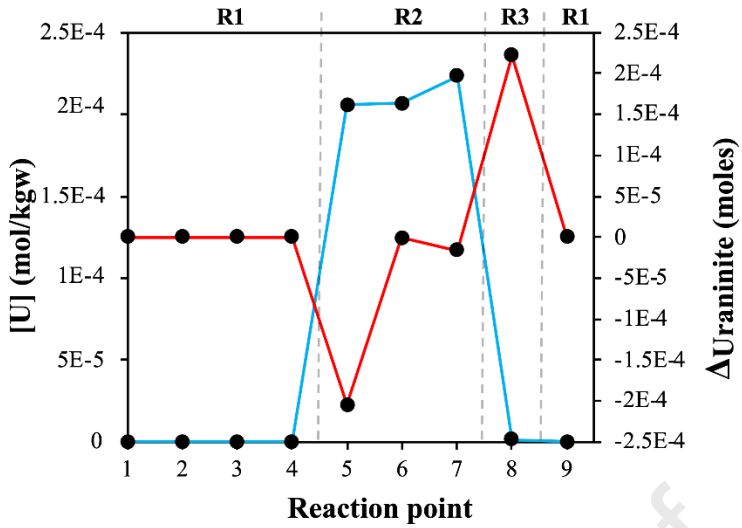

340

341 Figure 8: The variations of uraninite moles (in red) and uranium concentration in the solution (in blue) across the
342 three reservoirs.

343 The distribution of the uranium species in solution is depicted in Figure 9. In Reservoir 2,
344 U(VI) species predominate, featuring a variety of forms such as $UO_2(OH)^{3-}$ and $(UO_2)_3(OH)^{5+}$,
345 reflecting stability influenced by pH fluctuations. Conversely, in Reservoir 3, where uranium
346 concentration is significantly reduced due to uraninite precipitation under reductive conditions,
347 U(IV) species become predominant. Specifically, $U(OH)_2$ is the stable form observed
348 consistently across all five batch reaction stages, despite substantial variations in pH and pe.

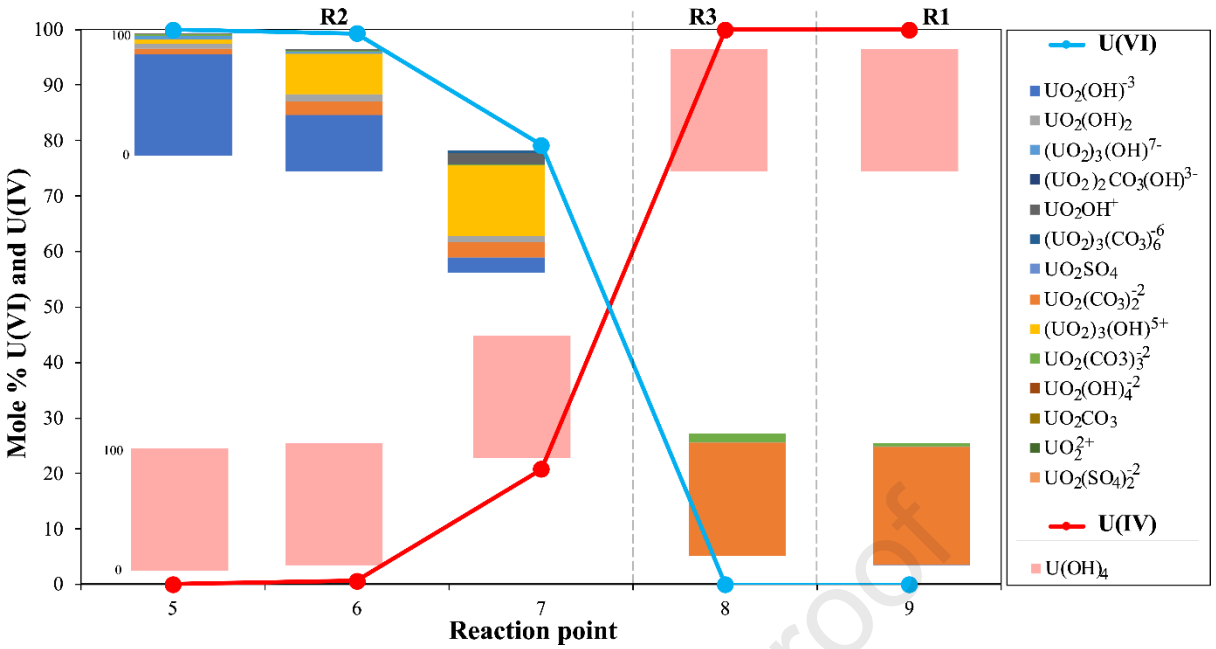

Figure 9: Relative proportions of U(VI) and U(IV) in the fluid phase for Reservoirs 2 and 3 for the base model. The dissolved species for U(VI) and their relative abundance are indicated as colored bands in the rectangles close to the blue line. The U(IV) species is $U(OH)_4$ for all points.

5.2 **Dependency of uranium mobility on Fluid/Rock (F/R) ratio**

The influence of the fluid/rock ratio on chemical parameters along the fluid path is shown in Figure 10. Initially, pH decreases consistently along the flow path for all F/R ratios, with the exception of a stabilization between points 8 and 9. This pH decline is particularly pronounced at lower F/R ratios (F/R = 0.01, 1 and 3; Fig. 10a). In Reservoir 1, the pe increases similarly across all F/R ratios (Fig. 10b). However, in Reservoir 2, the pe profile diverges, F/R ratios of 0.01 and 1 exhibit a significant drop followed by a subsequent increase, whereas F/R ratios of 3 and 100 display a continuous rise without a preceding decrease.

In the high fluid/rock ratio scenario (F/R = 100), the fluid geochemical evolution reveals distinct trends in both pH and pe compared to the base model. The pH decreases gradually from 11.6 at point 1 to 10.7 at point 8, followed by a slight increase to 10.8 at point 9. This more moderate pH decline can be attributed to a closer balance between proton-releasing and proton-

consuming reactions compared to the base model. In parallel, the pe rises from -2.5 at point 1 to a peak of 1.6 at point 6, then drops sharply to -8.2 at point 8, and remains low through point 9 (Fig. 10a and 10b). These notable deviations from the base model can be attributed to the high fluid volume compared to that of the rock, which facilitates extensive annite dissolution (Reaction 1), enabling the continuous increase in pe at the transition of Reservoir 1 to Reservoir 2. Additionally, the extensive pyrite dissolution (Reaction 5) in Reservoir 3 intensifies the reducing conditions, causing the pe to decline significantly to -8.2 at point 8.

In the scenarios with F/R ratios of 1 and 3, the pH behavior closely mirrors that observed in the base model. However, the pe profiles exhibit significant variations due to the different fluid-to-rock proportions.

For F/R = 1, the pe trend is similar to the base model but displays higher values between points 5 and 7 (Fig. 10b), indicating a relatively more oxidizing environment during this interval. The increased fluid volume relative to rock promotes enhanced oxidation reactions, such as the oxidation of ferrous iron and uranium species. Notably, uraninite dissolution reaches its peak at this fluid/rock ratio (Fig. 10b and 10d). The higher pe values suggest that the system has a greater capacity to consume electrons through these oxidation processes, resulting in more oxidizing conditions compared to the base model.

For F/R = 3, the pe pattern is similar to that of F/R = 100, with an initial increase followed by a decrease (Fig. 10b). However, the pe values remain higher from points 3 to 9 compared to the F/R = 100 scenario. This suggests that at F/R = 3, the system maintains more oxidizing conditions over a broader range of points. The balance between oxidation and reduction reactions is strongly influenced by the fluid/rock ratio, where the fluid volume is sufficient to drive oxidation reactions without overwhelming the system with reduced species from mineral

dissolution. As a result, the pe remains elevated for a longer portion of the fluid path, reflecting sustained oxidizing conditions.

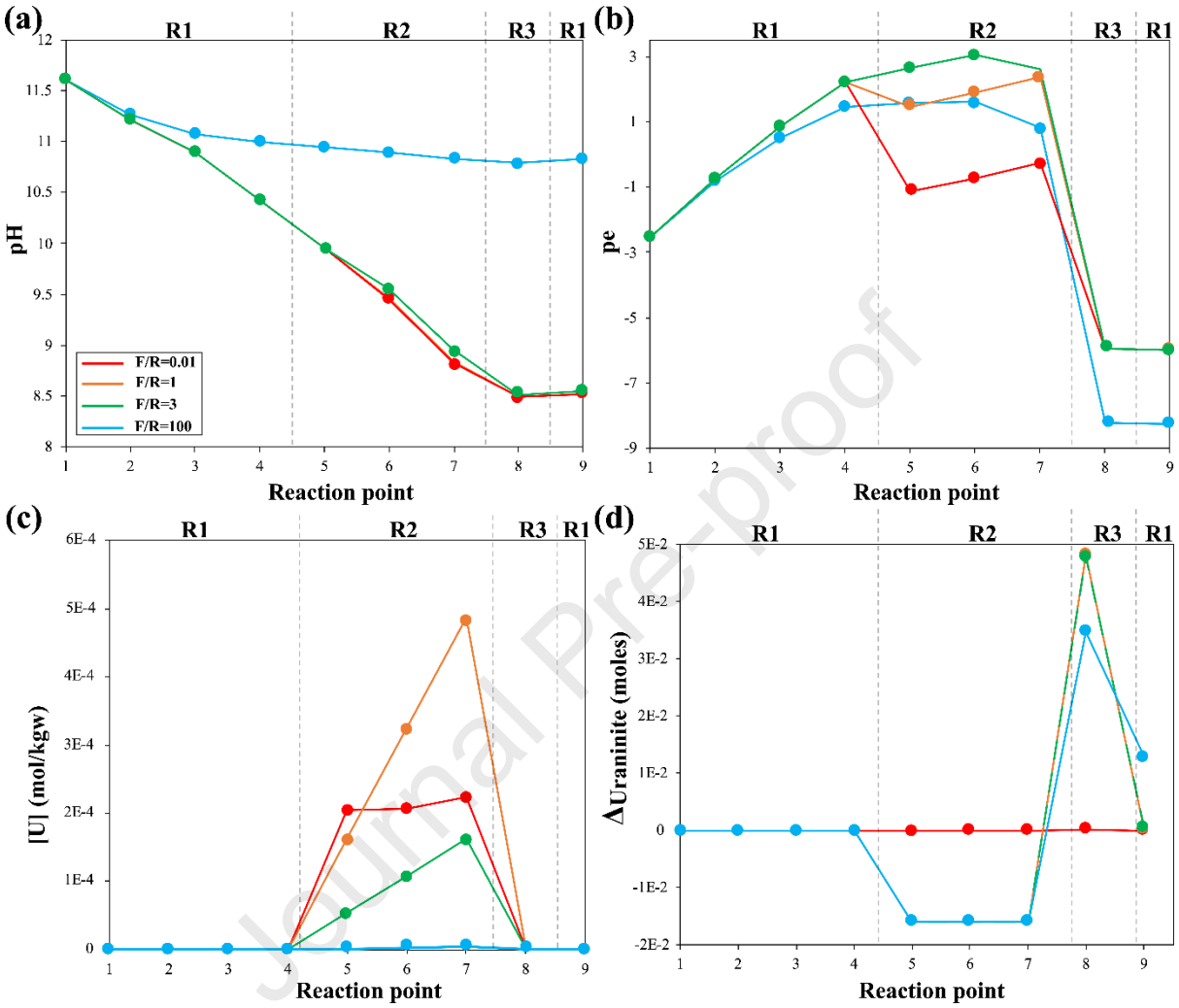

Figure 10: pH (a), pe (b), uranium concentration in the solution (c) and uraninite moles variation in the rock (d) along the reaction pathway (points 1 to 9) for various fluid/rock ratios. The red curve corresponds to the base model (it was presented on a larger scale in Figure 8).

The evolution of U concentration in solution (Fig. 10c) and the variation of uraninite amount in the rock (Fig. 10d) reveals a complex pattern. At point 5, an increase in the F/R ratio from 1 to 100 leads to a decrease in dissolved U due to a dilution effect. Points 6 and 7 show that the highest amount of dissolved U corresponds to F/R = 1 (Fig. 10c). The contents for F/R = 0.01 and 3 are not so different. For the rock, uraninite dissolution is very low for F/R = 0.01 (base

399 model, Fig. 10d) compared to higher F/R ratios. Uraninite dissolution (points 5, 6 and 7) and
400 precipitation (points 8 and 9) are both more pronounced for F/R ratios of 1, 3 and 100 than for
401 the base model (Fig. 10d).

402
403 These observations suggest a correlation between pe variability with respect to F/R ratios and
404 uraninite precipitation. Specifically, the lowest pe values at reaction points 8 and 9 correspond
405 to significant uraninite precipitation. This correlation is less obvious for uraninite dissolution
406 during which pe values vary more erratically and are less predictable. Nonetheless, the increase
407 in uraninite dissolution observed for high F/R ratios corresponds to high pe values (pe ≥ 1)
408 (Fig. 10b).

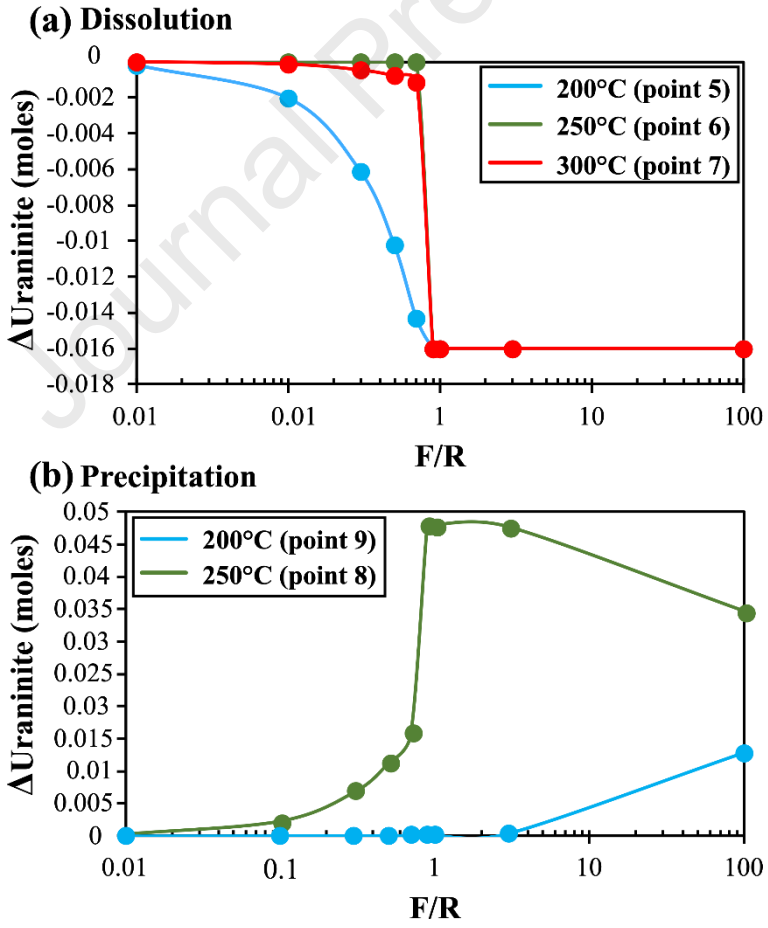

409

410 Figure 11: Variations of the uraninite moles in infiltrated rocks as a function of fluid/rock (F/R) ratios. Negative
411 values (a) indicate uraninite dissolution and positive values (b) indicate uraninite precipitation.

In Reservoir 2, for F/R ratios lower than 0.9, uraninite dissolution is lower at elevated temperatures (250°C-300°C) than at lower temperatures (200°C) (Fig. 11a). For F/R ratios higher than 0.9, the dissolution rate remains constant, with uraninite entirely dissolved (Fig. 11a). This feature may be explained by the fact that at high F/R ratios, oxidizing conditions are maintained in the uranium source, thereby sustaining the efficiency of uranium leaching. In Reservoir 3 (Fig. 11b), there is an increase in uraninite precipitation for F/R ratios lower than 0.9, followed by a decrease in precipitation rate. This behavior contrasts with Reservoir 1 (point 9, Fig. 11b), where uraninite precipitation increases for F/R ratios higher than 3.

5.3 **Influence of the initial redox state**

To assess the impact of the reservoir redox state on pH, pe, variation of uraninite amount in the rock and U concentration in solution along the fluid path, magnetite was introduced into Reservoir 1 (Fig. 12; refer to section 4.4 for more details). These tests were conducted in the conditions of the base model (F/R = 0.01).

First, addition of magnetite had minimal influence on the pH trend (Fig. 12a). On the other hand, significant fluctuations in pe values are observed, consistently remaining negative and reaching a pe value of -3 (maximum value for reaction point 7), indicative of the strong redox buffering capacity of magnetite (Fig. 12b). These variations significantly influenced U mobilization and subsequent precipitation, as evidenced by the patterns in U concentrations and uraninite behavior along the fluid pathway (Fig. 12c and 12d). At points 5 and 6, uraninite dissolution was low but slightly increased at point 7 (Fig. 12b and 12c). Similar patterns are observed in U concentration in solution (Fig. 12c). No significant changes in pH, pe, U concentration and uraninite quantities occurred when increasing the magnetite content from 0.5 to 1.6 wt.% in Reservoir 1.

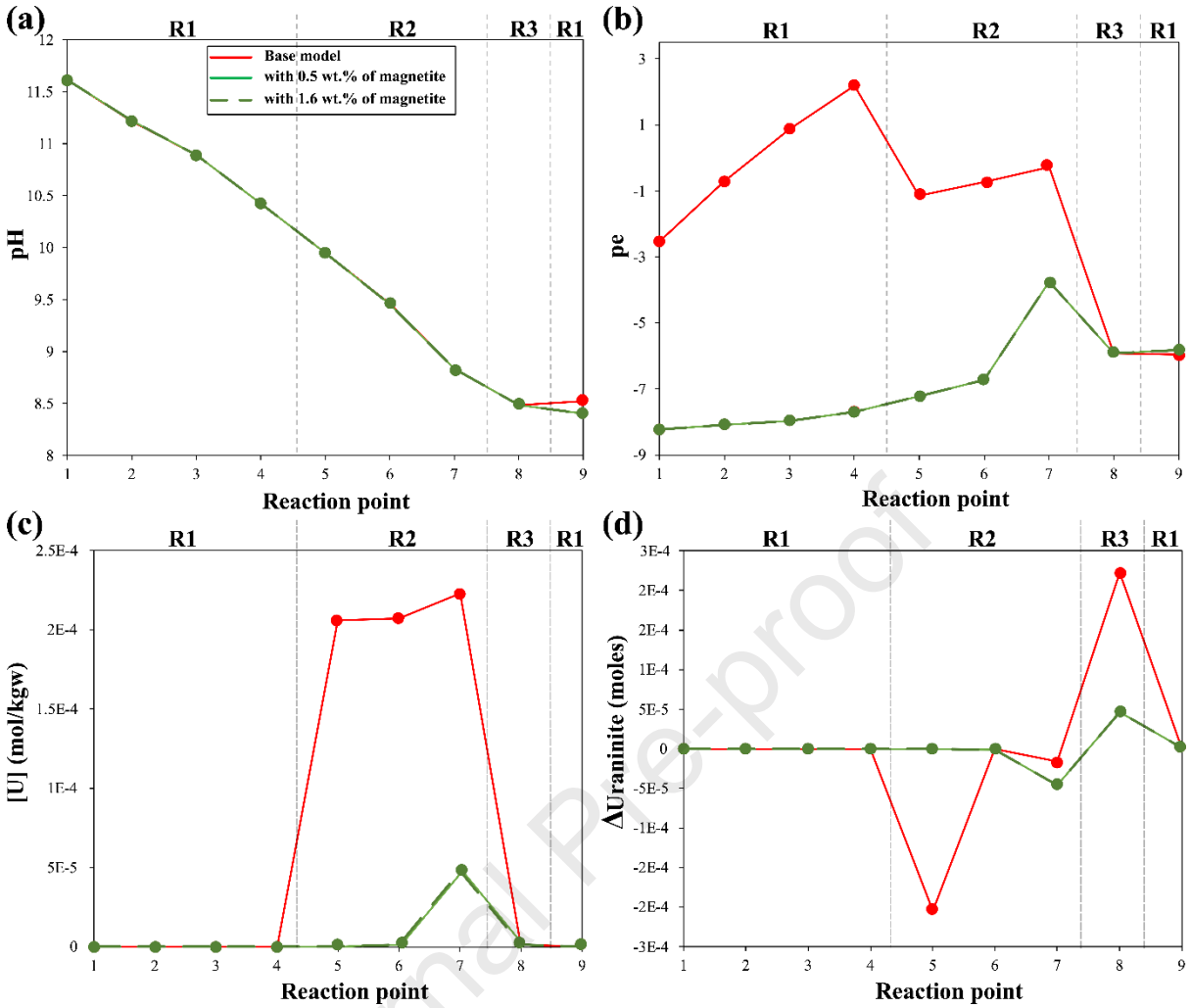

Figure 12: Effects of adding magnetite in Reservoir 1 on pH (a), pe (b), U concentration in solution (c) and uraninite moles variations in the rock (d) along the fluid journey.

The reducing conditions due to the presence of magnetite also exert a significant influence on the speciation of U in the solution and the distribution of its oxidation states (Fig. 13). In contrast to experiments conducted without magnetite in Reservoir 1 (Fig. 9), U in solution is predominantly in the U(IV) state. U(VI) species represent only about 3% of the U species at point 7. U(IV) is primarily present as $U(OH)_4$, while the very low amount of U(VI) in the solution is mostly associated with carbonate species (Fig. 13).

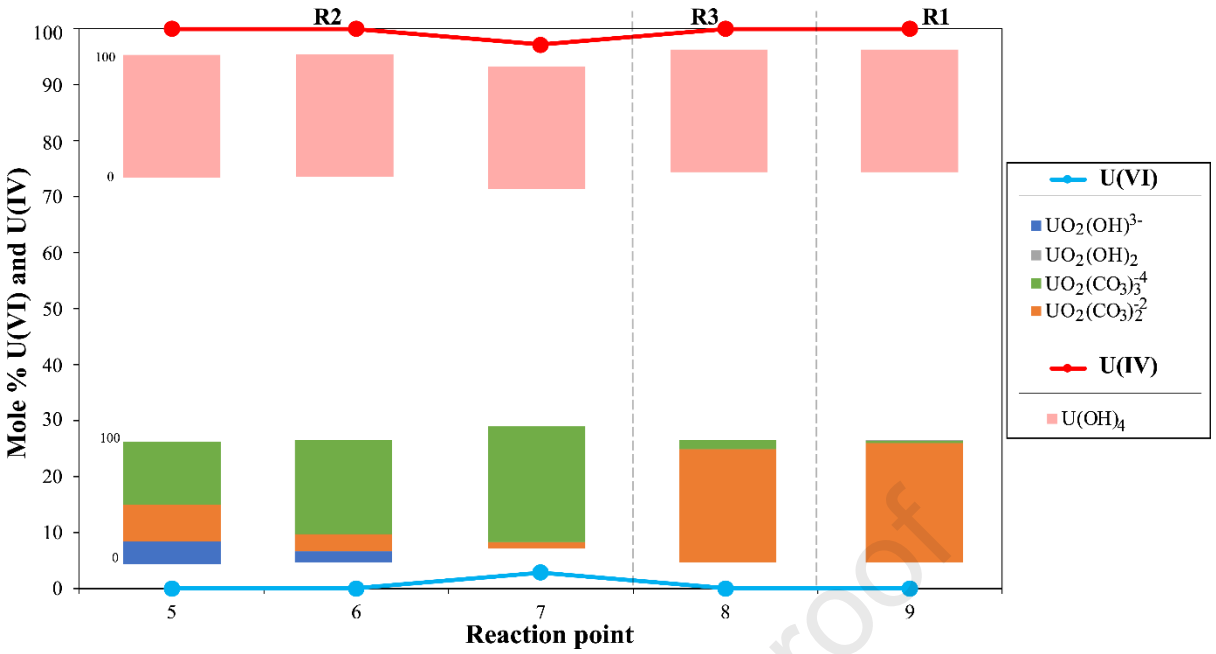

Figure 13: Evolution of U(VI) and U(IV) concentrations as percentages in the fluid for the model with 0.5 wt.% magnetite in Reservoir 1. The uranium species are indicated for both valences.

6. Discussion

6.1 Oxidation state of U

Direct comparisons using precise pe or Eh values between our results and other research findings are challenging due to the unique numerical approach we employed and the limited number of studies addressing this issue. However, comparisons can be made considering general trends in the oxidation state of U.

In our base model (F/R ratio of 0.01), pe values of -1.14, -0.73, and -0.27 were calculated at 200°C, 250°C, and 300°C, respectively, in Reservoir 2 (Fig. 6), indicating moderately reducing conditions that promote the dissolution of primary magmatic uraninite (Fig. 8). Despite a trend towards less reducing conditions with increasing temperature, the fraction of U(VI) in the aqueous phase decreases from 200°C to 300°C (points 5 to 7, Fig. 9). This appears

463 counterintuitive since uraninite is more stable under reducing conditions (Langmuir, 1978),
464 and U(VI) typically dominates in oxidizing environments (Langmuir, 1978; Janeczek and
465 Ewing, 1992; Artinger et al., 2002).

466 However, this conventional understanding has been challenged by several studies. For
467 example, Timofeev et al. (2018) demonstrated that uranium can remain mobile under reducing
468 conditions in chloride-rich brines via the formation of UCl_4° complexes, particularly at Cl
469 concentrations of 0.1–1 mol/kg, pH 1.5–2.6 (at 25°C), and temperatures of 250–350°C. These
470 conditions favor uranium transport through chloride complexation. In contrast, our model fluid
471 contains much lower Cl concentrations (1.13×10^{-5} mol/kg), higher pH (8.5–11.6), and lower
472 temperature ranges (25–300°C), which do not support U-Cl complexation. As Timofeev et al.
473 (2018) highlighted, "the ideal fluid for moving uranium is hot, chloride-rich, and highly
474 acidic", whereas our conditions, being closer to the opposite end of the spectrum, explain why
475 uranium mobility in our study is not driven by chloride complexation. Another complexation
476 that could play a crucial role in uranium mobility is calcium-uranyl-carbonate (Ca-U(VI)-CO_3)
477 complexes. Previous studies have demonstrated that ternary complexes such as $CaUO_2(CO_3)_3^{2-}$
478 and $Ca_2UO_2(CO_3)_3(aq)$ dominate uranium(VI) speciation in calcium-rich environments,
479 enhancing uranium solubility and mobility under neutral to alkaline pH conditions and
480 temperatures that varies from 20°C to 80°C (Fox et al., 2005; Maia et al., 2021).

481 Although $CaUO_2(CO_3)_3^{2-}$ typically exhibits a peak in uranium(VI) speciation around pH 8 at
482 25°C (Fig. 5c), no significant concentrations of Ca-U complexes were detected in our solutions
483 (Fig. 9). This absence can be attributed to the lack of abundant calcium in our granitic system
484 (Fig. 4), coupled with the high temperatures (200–300°C) encountered in our experiments.
485 Such elevated temperatures inhibit the formation of $CaUO_2(CO_3)_3^{2-}$, as previously reported by
486 Maia et al. (2021).

Additionally, Janeczek and Ewing (1992) observed that uraninite dissolution can occur under hydrothermal reducing conditions at sites such as Oklo (Gabon) and Cigar Lake (Canada), even at moderate temperatures (~200°C) in the presence of saline, moderately acidic solutions. Their study also showed that uraninite can crystallize incorporating both U(IV) and U(VI) states, challenging the assumption that post-formational oxidation is always necessary. On the other hand, uraninite precipitation can occur without the typical reduction step from U(VI) to U(IV), particularly in environments rich in silica (Pan et al., 2021). This non-reductive precipitation involves the formation of uranyl silicate complexes, where U binds directly as uranyl (UO_2^{2+}) in the presence of silica. Therefore, these studies provide some clues to explain the moderate reducing state we observed during U leaching from the pluton apical zone (Reservoir 2). Such moderate reducing conditions encountered with a F/R ratio of 0.01, disappear with a higher F/R ratio (≥1) which imposed oxidizing conditions (Fig. 10b). Following the fluid pathway, by the time the fluid reaches Reservoir 3 (point 8), reducing conditions controlled by pyrite are calculated, inducing a classical behavior of U aligning with the oxidation state: uraninite precipitates and U(VI) concentration decreases in solution (almost reaching zero), with the remaining aqueous U being predominantly in the U(IV) state (Fig. 6 and Fig. 9).

The introduction of magnetite in Reservoir 1 significantly decreases the oxidative potential, shifting from mildly reducing conditions in the base model to moderately to strongly reducing conditions all along the fluid pathway (Fig. 12b). This alteration strongly influences U speciation, promoting a predominance of U(IV) in the aqueous phase within Reservoir 2 (Fig. 13).

The contrast in oxidation states between the base model (without magnetite in Reservoir 1) and the experiments with magnetite in Reservoir 1 (Fig. 12) can be discussed in relation to THCC (Thermo-Hydro-Chemical Coupling) results from Carnahan (1986). This author used two

different fluid sources to study how the redox state of the environment affects the behavior of U in the solution. For an oxidized fluid, with a pH of 6 and an Eh of 0.0V at 90°C, Carnahan (1986) showed that U species include both U(VI) and U(IV) complexes. The predominant species are U(VI) carbonate complexes such as UO_2CO_3 and $UO_2(CO_3)_2^{2-}$, with low concentrations of U(IV) hydroxide. In contrast, in his scenario using a reduced fluid, with a pH of 10 and an Eh of -0.4 V at 90°C, he showed that the dominant U species of U(IV) is $U(OH)_4$. This indicates that under reducing conditions and high pH, U(IV) species like uraninite tend to dissolve but the soluble U remains predominantly in the U(IV) state. Even though pH and temperature conditions are different, our results accord with the ones of Carnahan (1986). Indeed, in the base model, which features mildly reducing conditions (not far from Eh of 0.0 V used by Carnahan (1986)), both U(VI) and U(IV) coexist, with higher proportion of U(VI) in Reservoir 2 and a predominance of carbonate species (Fig. 9). Conversely, in the model with magnetite in Reservoir 1, U(IV) is the predominant species, represented by $U(OH)_4$ (Fig. 13), similarly to the Carnahan (1986) reduced source model.

Uranium leaching from Reservoir 2 is more efficient in the base model than in the test with magnetite in Reservoir 1 (Fig. 12d). Conditions in the base model favor the formation of U complexes in solution, enhancing U mobility (Fig. 12c). Conversely, magnetite in Reservoir 1 leads to the formation of less soluble U species, limiting U leaching from Reservoir 2 (Fig. 12c and 12d). This observation is also consistent with Carnahan (1986), who highlighted high U mobility for oxidizing fluids.

6.2 Fluid/Rock ratio and uranium recovery rate: insight into natural systems

To visualize the efficiency of the fluid/rock interaction system modeled here, we defined the Uranium Recovery Rate (URRa), with two types. URRa1 compares the mass of uranium

precipitated with the total mass of uranium in the source, whereas URRa2 compares the uranium precipitated with the uranium leached from the source. Thus, URRa1 provides information on the efficiency of the whole system, whereas URRa2 informs on the efficiency of the entrapment only.

In Figure 14 we observe that the URRa1 and URRa2 are dependent on the F/R ratio. For F/R ratios lower than 0.9, the horizontal red line shows that nearly all the dissolved uraninite from Reservoir 2 is precipitated in Reservoir 3 (URRa2 = 100%). For F/R ratio higher than 0.9, the efficiency of uraninite precipitation decreases (slope of the red curve in Fig. 14). The abrupt increase of URRa1 around the F/R ratio of 0.9 (blue curve in Fig. 14) is controlled by the efficiency of uraninite dissolution in the source rather than the uraninite precipitation rate in the trap. At a F/R of 0.9, URRa1 is maximal around 97.5%. The remaining uranium is transported away in the solution and may precipitate further, e.g., at reaction point 9 (Fig. 11b).

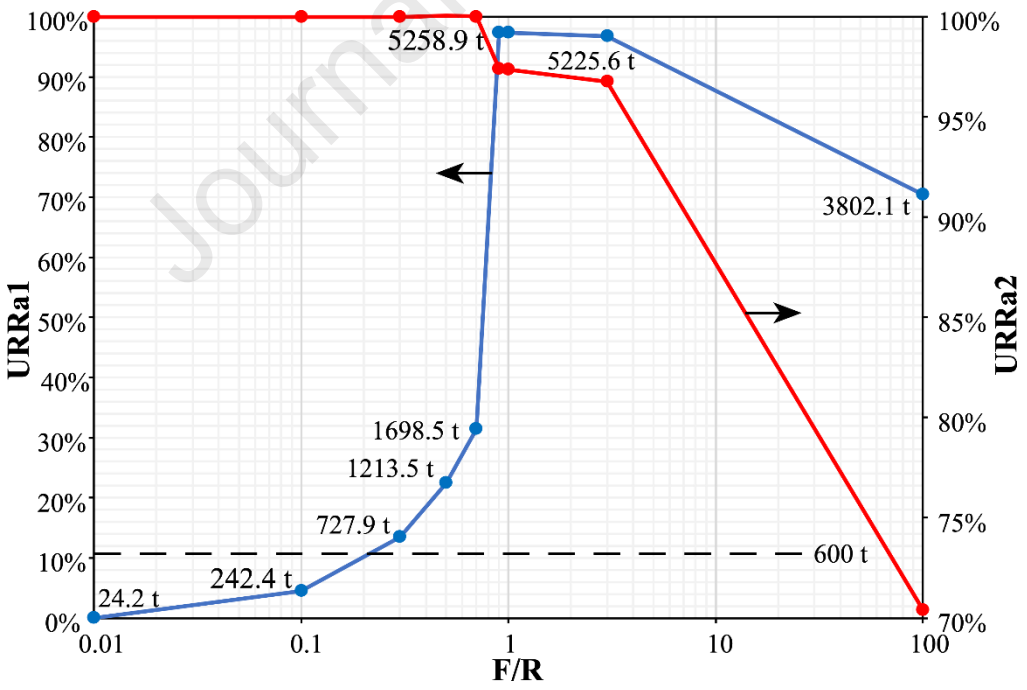

Figure 14: Uranium Recovery Rates (URRa1, left y-axis, blue curve and URRa2, right y-axis, red curve) as a function of F/R ratio: (i) URRa1 represents the mass of uranium precipitated at point 8 divided by the sum of the initial uranium mass at points 5, 6 and 7; (ii) URRa2 represents the mass of uranium precipitated at point 8 divided

by the sum of the dissolved uranium mass from points 5, 6 and 7. The mass in tons plotted along the blue curve corresponds to the calculated mass of uranium precipitated at point 8 (deposit) considering an initial content of 5400 tons of uranium (contained in primary magmatic uraninite) in the source (see text for details).

Our calculations regarding uranium recovery can be compared with the estimates of Ballouard et al. (2017) on the Guérande U metallogenic model. According to these authors, the total mass of uranium leachable from the uraninite-bearing apical zone of the pluton is 5400 tons. Around 600 tons of U were actually mined at the Pen Ar Ran mine (Fig. 1d). The U mined represents about 11% of the available U. This value of 11% corresponds to a theoretical F/R ratio of 0.2 (obtained by simple reading on the blue curve in Figure 14). Obviously, such value of 11% is lower than the actual URRa1 value of the Guérande system given that the total amount of uranium deposited is higher than the uranium mined. To estimate the URRa1 of the Guérande system, one has first to estimate the F/R ratio, for example using isotopic data. Dusséaux et al. (2019) and Ballouard et al. (2015) provide such stable isotope data, respectively in the hydrogen and the oxygen systems. Both systems show isotopic alteration in the granite-deformed cupola, indicative of rather high F/R ratios, likely above 0.5, despite no precise quantification. The fact that the oxygen isotope values are not buffered to constant values indicates that the F/R ratio in the granite cupola is lower than 3 (e.g., Boulvais et al., 1998). A reasonable range of F/R ratios for the Guérande system is then between 0.5 and 3. Reporting these values in Figure 14 indicates a range of URRa1 values between 22% and 97% (reading on the blue curve). In the end, one can estimate that between 1213 tons and 5225 tons of uranium may have precipitated in the Guérande system. This crude calculation based on the comparison between our URRa1 and data from the Guérande systems shows that the uranium actually mined at Guérande represents a small fraction of the uranium that was likely deposited. At first sight, it could be good news for uranium prospection. However, our reasoning provides no information on the morphology of the potential deposit, highly concentrated in a small zone

575 (high concentration, low volume) or diluted in a large zone (low concentration, high volume).
576 It has thus to be complemented by geological constraints.

577 **6.3 Application of the TH-C approach to other U mineralized systems**

578 Our modeling provides insights into U mobilization and precipitation mechanisms within a
579 detachment-related mineralization system associated with the emplacement of granitic melts.
580 However, it is crucial to acknowledge the limitations of these models in accurately representing
581 the complexity and scale of natural geological settings. First, the temperature range of the
582 LLNL chemical database used in our model is limited to below 300°C, whereas some
583 mineralization has been documented to occur up to 350°C for the South Armorican case
584 (Ballouard et al., 2017). Furthermore, the LLNL database does not allow independent
585 adjustment of pressure. Instead, it assumes a constant pressure of 1 bar for temperatures up to
586 100°C and saturation pressure for temperatures up to 300°C. This simplification may not fully
587 capture the complex pressure dynamics in natural systems, although the difference between
588 this assumed pressure and the actual fluid pressures indicated in the hydrodynamic model
589 appears to be minimal (Fig. 2b).

590 Notwithstanding these constraints, the TH-C approach presented here offers time efficiency
591 and a more refined chemical analysis compared to the methods that fully coupled transport
592 equations with chemical reactions (Steefel et al., 2005). Additionally, our study extends the
593 existing knowledge base by conducting numerical modeling on U mobility across a wide
594 temperature range from 25°C to 300°C. This aspect of our research addresses a gap in the
595 literature, which has predominantly focused on U geochemistry at low temperatures.

596 Our TH-C modeling has the potential to investigate a wide spectrum of U deposits, particularly
597 those where the trapping temperatures of the mineralized fluids are below 300°C. This includes
598 the high-grade unconformity-related U deposits, which are situated at, above, or below a major

599 unconformity. In the Athabasca system (Canada), this boundary separates the Archean to
600 Paleoproterozoic basement and Proterozoic sedimentary sequences (Ruzicka, 1995; Jefferson
601 et al., 2007; Dahlkamp, 2010). Studies have consistently indicated that the formation
602 temperatures of these unconformity-related U deposits remain under 300°C. For example,
603 Cuney (2010) and Polito et al. (2011) point to formation temperatures around 200°C in the
604 Alligator Rivers Uranium Field. Likewise, Jaireth et al. (2016) reported temperature ranges of
605 180°C to 250°C during the peak diagenesis of sandstone units. Cloutier et al. (2009) and
606 Kojima et al. (1994) identified similar temperatures up to 250°C, associated with fluid
607 interactions during muscovite alteration and within Canadian deposits, respectively. Richard et
608 al. (2013) detailed trapping temperatures for U mineralizing brines in the Athabasca Basin
609 between 100°C and 150°C for NaCl-rich brines and 80°C to 140°C for $CaCl_2$-rich brines.
610 Collectively, these findings support a formation temperature in the range of 80-250°C for
611 unconformity-related high-grade uranium mineralization, well within the applicable scope of
612 our TH-C approach.

613 Another type of U mineralization is vein-type deposits. As described by Ruzicka (1993), vein-
614 type deposits are identified as epigenetic concentrations of U, predominantly as pitchblende
615 and coffinite, situated within fractures, shear zones and stockworks. These deposits are
616 typically hosted by granitic or syenitic rocks and can also be found in sheared or mylonitized
617 rocks, metamorphosed sedimentary complexes. The formation of these deposits is generally
618 associated with the late phases of orogenic cycles, where changes in fluid pH, pe, pressure and
619 temperature play pivotal roles (Ruzicka, 1993). For example, in the Jáchymov deposits,
620 deposition of pitchblende occurred at temperatures between 370°C and 470°C. In contrast, the
621 Beaverlodge U district in northern Saskatchewan formed at temperatures between 100°C and
622 250°C (Liang et al., 2017). These temperature ranges highlight the diversity in conditions under

623 which vein-type uranium mineralization can occur, reflecting variations in geological settings
624 and fluid/rock interactions, and challenging the application of our TH-C numerical modeling.

625 ## 7. Conclusions

626 The thermo-hydro-chemical (TH-C) numerical modeling approach employed in this study
627 appears effective in simulating uranium mobilization associated with syn-kinematic granite
628 emplacement in detachment zones. A key finding is that uranium mobility is not solely driven
629 by the oxidizing characteristics of percolating surface-derived fluids. Our TH-C modeling
630 reveals significant changes in the redox potential of these fluids as they traverse the crust. By
631 the time these surface-derived fluids reach uranium-rich source rocks, their pe adjusts towards
632 more neutral or slightly reducing conditions. Remarkably, even after this evolution, the fluids
633 retain the capacity to dissolve uranium, subsequently precipitating it in more reducing
634 environments. Furthermore, our calculations indicate persistent uranium dissolution in the
635 presence of magnetite, which enhances fluid reducing properties, resulting in distinct species,
636 notably U(IV) in the aqueous phase.

637 Our results highlight the complexity of uranium mobilization, indicating that factors beyond
638 simple oxidation-reduction dynamics play major roles. Temperature, pH, and fluid/rock (F/R)
639 ratios emerge as critical determinants of this process. Particularly, the fluid/rock (F/R) ratio
640 significantly influences uranium leaching, with high ratios enhancing uranium extraction from
641 source rocks. Interestingly, an optimal F/R ratio of approximately 1 maximizes both leaching
642 efficiency from the source and precipitation efficiency in the traps. Below this F/R ratio,
643 dissolution efficiency decreases, whereas above it, precipitation efficiency decreases.

644 Our TH-C approach is compatible with geologically-based conceptual models and allows for
645 the quantification of uranium mobilities, such as those seen in granite-related uranium deposits
646 (e.g., the Guérande U-bearing system in the Armorican Massif, West European Variscan
647 chain). Furthermore, this approach appears to be robust for up to 300°C uranium-mineralizing
648 systems. While these findings are promising, extend this methodology to higher temperatures,
649 depends on the availability and accuracy of thermodynamic data. Therefore, expanding
650 thermodynamic databases through targeted laboratory experiments is crucial to improve the
651 robustness of the modeling approach.

652 **CRediT authorship contribution statement**

653 Khaled Bock: Writing – review and editing, Writing – original draft, Visualization,
654 Methodology, Investigation, Data curation, Conceptualization. Yannick Branquet: Writing –
655 review and editing, Supervision, Investigation, Validation, Funding acquisition,
656 Conceptualization. Olivier Pourret: Writing – review and editing, Formal analysis,
657 Conceptualization. Philippe Boulvais: Writing – review and editing, Supervision,
658 Investigation, Validation, Funding acquisition, Conceptualization.

659

660 **Declaration of competing interest**

661 The authors declare that they have no known competing financial interests or personal
662 relationships that could have appeared to influence the work reported in this paper.

Data availability

Datasets related to this article are available on request from the corresponding author.

Acknowledgments

This study was supported by the NEEDS consortium (URAMOD project). Thibault Duretz is thanked for continuous discussions.

References

Abdelouas, A. 2006. Uranium Mill Tailings: Geochemistry, Mineralogy, and Environmental Impact. Elements, 2(6), 335–341. https://doi.org/10.2113/gselements.2.6.335

Artinger, R., Rabung, T., Kim, J. I., Sachs, S., Schmeide, K., Heise, K. H., Bernhard, G., and Nitsche, H. 2002. Humic colloid-borne migration of uranium in sand columns. Journal of Contaminant Hydrology, 58(1–2), 1–12. https://doi.org/10.1016/S0169-7722(02)00032-3

Ballouard, C., Boulvais, P., Poujol, M., Gapais, D., Yamato, P., Tartèse, R., and Cuney, M. 2015. Tectonic record, magmatic history and hydrothermal alteration in the Hercynian Guérande leucogranite, Armorican Massif, France. Lithos, 220–223, 1–22. https://doi.org/10.1016/j.lithos.2015.01.027

Ballouard, C., Poujol, M., Boulvais, P., Mercadier, J., Tartèse, R., Venneman, T., Deloule, E., Jolivet, M., Kéré, I., Cathelineau, M., and Cuney, M. 2017. Magmatic and hydrothermal behavior of uranium in syntectonic leucogranites: The uranium mineralization associated with the Hercynian Guérande granite (Armorican Massif, France). Ore Geology Reviews, 80, 309–331. https://doi.org/10.1016/j.oregeorev.2016.06.034

Bock, K., Branquet, Y., Boulvais, P., & Duretz, T. 2024. Surface-derived fluid percolation along detachment systems enhanced by syn-kinematic granites: Uranium mineralization

as an application. BSGF - Earth Sciences Bulletin, 195, 13. https://doi.org/10.1051/bsgf/2024010

Boulvais, P., Fourcade, S., Gruau, G., Moine, B., & Cuney, M. (1998). Persistence of pre-metamorphic C and O isotopic signatures in marbles subject to Pan-African granulite-facies metamorphism and U–Th mineralization (Tranomaro, Southeast Madagascar). Chemical Geology, 150(3-4), 247-262.

Carnahan, C. L. 1986. Simulation of Uranium Transport with Variable Temperature and Oxidation Potential: The Computer Program Thcc. MRS Proceedings, 84, 713. https://doi.org/10.1557/PROC-84-713

Cathelineau, M., Boiron, M. C., Holliger, P., and Poty, B. 1990. Metallogenesis of the French part of the Variscan orogen. Part II: Time-space relationships between U, Au and Sn-W ore deposition and geodynamic events—mineralogical and U-Pb data. Tectonophysics, 177(1-3), 59-79.

Cloutier, J., Kyser, K., Olivo, G. R., Alexandre, P., and Halaburda, J. 2009. The Millennium Uranium Deposit, Athabasca Basin, Saskatchewan, Canada: An Atypical Basement-Hosted Unconformity-Related Uranium Deposit. Economic Geology, 104(6), 815–840. https://doi.org/10.2113/gsecongeo.104.6.815

Collet, A., Regnault, O., Ozhogin, A., Imantayeva, A., and Garnier, L. 2022. Three-dimensional reactive transport simulation of Uranium in situ recovery: Large-scale well field applications in Shu Saryssu Bassin, Tortkuduk deposit (Kazakhstan). Hydrometallurgy, 211, 105873. https://doi.org/10.1016/j.hydromet.2022.105873

Cuney, M. 1978. Geologic environment, mineralogy, and fluid inclusions of the Bois Noirs-Limouzat uranium vein, Forez, France. Economic Geology, 73(8), 1567–1610. https://doi.org/10.2113/gsecongeo.73.8.1567

709 Cuney, M. 2009. The extreme diversity of uranium deposits. Mineralium Deposita, 44(1), 3–
710 9. https://doi.org/10.1007/s00126-008-0223-1
711 Cuney, M. 2010. Evolution of Uranium Fractionation Processes through Time: Driving the
712 Secular Variation of Uranium Deposit Types. Economic Geology, 105(3), 553–569.
713 https://doi.org/10.2113/gsecongeo.105.3.553
714 Cuney, M., Friedrich, M., Blumenfeld, P., Bourguignon, A., Boiron, M. C., Vigneresse, J. L.,
715 and Poty, B. 1990. Metallogenesis in the French part of the Variscan orogen. Part I: U
716 preconcentrations in pre-Variscan and Variscan formations — a comparison with Sn, W
717 and Au. Tectonophysics, 177(1–3), 39–57. https://doi.org/10.1016/0040-1951(90)90273-
718 B
719 Cuney, M., Kyser, K., Mineralogical Association of Canada, and Society for Geology Applied
720 to Mineral Deposits (Eds.). 2009. Recent and not-so-recent developments in uranium
721 deposits and implications for exploration ; short course co-sponsored by the SGA and
722 MAC, and delivered at the joint annual meeting of the GAC-MAC-SEG-SGA, Québec
723 City, Québec, 24—25 May, 2008. Mineralogical Association of Canada.
724 Curtis, G. P., Davis, J. A., and Naftz, D. L. 2006. Simulation of reactive transport of
725 uranium(VI) in groundwater with variable chemical conditions. Water Resources
726 Research, 42(4), 2005WR003979. https://doi.org/10.1029/2005WR003979
727 Dahlkamp, F. J. 2010. Uranium Deposits of the World: USA, and Latin America. 499.
728 Descriptive uranium deposit and mineral system models. 2020. IAEA.
729 Dusséaux, C., Gébelin, A., Boulvais, P., Gardien, V., Grimes, S., & Mulch, A. 2019. Meteoric
730 fluid-rock interaction in Variscan shear zones. Terra Nova, ter.12392.
731 https://doi.org/10.1111/ter.12392
732 Eldursi, K., Branquet, Y., Guillou-Frottier, L., and Marcoux, E. 2009. Numerical investigation
733 of transient hydrothermal processes around intrusions: Heat-transfer and fluid-circulation

734 controlled mineralization patterns. Earth and Planetary Science Letters, 288(1–2), 70–83.
735 https://doi.org/10.1016/j.epsl.2009.09.009
736 Eldursi, K., Branquet, Y., Guillou-Frottier, L., Martelet, G., and Calcagno, P. 2018. Intrusion-
737 Related Gold Deposits: New insights from gravity and hydrothermal integrated 3D
738 modeling applied to the Tighza gold mineralization (Central Morocco). Journal of African
739 Earth Sciences, 140, 199–211. https://doi.org/10.1016/j.jafrearsci.2018.01.011
740 Finch, R. J., and Ewing, R. C. 1992. The corrosion of uraninite under oxidizing conditions.
741 Journal of Nuclear Materials, 190, 133–156. https://doi.org/10.1016/0022-
742 3115(92)90083-W
743 Fox, P. M., Davis, J. A., & Zachara, J. M. (2006). The effect of calcium on aqueous
744 uranium(VI) speciation and adsorption to ferrihydrite and quartz. Geochimica et
745 Cosmochimica Acta, 70(6), 1379–1387. https://doi.org/10.1016/j.gca.2005.11.027
746 Freeze, R. A., and Cherry, J. A. 1979. Groundwater prentice-hall. Englewood Cliffs, NJ, 176,
747 161-177
748 Grenthe, I., Fuger, J., Konings, R. J., Lemire, R. J., Muller, A. B., Nguyen-Trung, C., &
749 Wanner, H. (1992). Chemical thermodynamics of uranium (Vol. 1, p. 735). Amsterdam:
750 Elsevier.
751 Harcouët-Menou, V., Guillou-Frottier, L., Bonneville, A., Adler, P. M., and Mourzenko, V.
752 2009. Hydrothermal convection in and around mineralized fault zones: Insights from two-
753 and three-dimensional numerical modeling applied to the Ashanti belt, Ghana. Geofluids,
754 9(2), 116–137. https://doi.org/10.1111/j.1468-8123.2009.00247.x
755 Harris, N. B. W., & Inger, S. 1992. Trace element modelling of pelite-derived granites.
756 Contributions to Mineralogy and Petrology, 110(1), 46–56.
757 https://doi.org/10.1007/BF00310881

758 Jaireth, S., Roach, I. C., Bastrakov, E., and Liu, S. 2016. Basin-related uranium mineral systems
759 in Australia: A review of critical features. Ore Geology Reviews, 76, 360–394.
760 https://doi.org/10.1016/j.oregeorev.2015.08.006
761 Janeczek, J., and Ewing, R. C. 1992. Dissolution and alteration of uraninite under reducing
762 conditions. Journal of Nuclear Materials, 190, 157–173. https://doi.org/10.1016/0022-
763 3115(92)90084-X
764 Jefferson, C. W., Thomas, D. J., Gandhi, S. S., Ramaekers, P., Delaney, G., Brisbin, D., Cutts,
765 C., Portella, P., & Olson, R. A. 2007. Unconformity-associated uranium deposits of the
766 Athabasca Basin, Saskatchewan and Alberta (588; p. 588).
767 https://doi.org/10.4095/223744
768 Kojima, S., Takeda, S., and Kogita, S. 1994. Chemical factors controlling the solubility of
769 uraninite and their significance in the genesis of unconformity-related uranium deposits.
770 Mineralium Deposita, 29(4). https://doi.org/10.1007/BF00191041
771 Komninou, A., & Sverjensky, D. A. 1996. Geochemical modeling of the formation of an
772 unconformity-type uranium deposit. Economic Geology, 91(3), 590–606.
773 https://doi.org/10.2113/gsecongeo.91.3.590
774 Kříbek, B., Žák, K., Dobeš, P., Leichmann, J., Pudilová, M., René, M., Scharm, B., Scharmová,
775 M., Hájek, A., Holeczy, D., Hein, U. F., and Lehmann, B. 2009. The Rožná uranium
776 deposit (Bohemian Massif, Czech Republic): Shear zone-hosted, late Variscan and post-
777 Variscan hydrothermal mineralization. Mineralium Deposita, 44(1), 99–128.
778 https://doi.org/10.1007/s00126-008-0188-0
779 Labrousse, L., Huet, B., Le Pourhiet, L., Jolivet, L., and Burov, E. 2016. Rheological
780 implications of extensional detachments: Mediterranean and numerical insights. Earth-
781 Science Reviews, 161, 233–258. https://doi.org/10.1016/j.earscirev.2016.09.003
782 Langmuir, D. (1997). Aqueous environmental geochemistry.

783 Langmuir, D. 1978. Uranium solution-mineral equilibria at low temperatures with applications
784 to sedimentary ore deposits. Geochimica et Cosmochimica Acta, 42(6), 547-569.
785 Lee, K., Fetter, C. W., and McCray, J. E. 2003. Hydrogeology laboratory manual (2nd ed).
786 Pearson Education.
787 Liang, R., Chi, G., Ashton, K., Blamey, N., and Fayek, M. 2017. Fluid compositions and P-T
788 conditions of vein-type uranium mineralization in the Beaverlodge uranium district,
789 northern Saskatchewan, Canada. Ore Geology Reviews, 80, 460–483.
790 https://doi.org/10.1016/j.oregeorev.2016.07.012
791 M. Cuney. 1978 Geologic environment, mineralogy, and fluid inclusions of the Bois Noirs-
792 Limouzat uranium vein, Forez, France. Economic Geology. 73 (8): 1567–1610.
793 doi: https://doi.org/10.2113/gsecongeo.73.8.1567
794 Maia, F. M. S., Ribet, S., Bailly, C., Grivé, M., Madé, B., & Montavon, G. (2021). Evaluation
795 of thermodynamic data for aqueous Ca-U(VI)-CO3 species under conditions
796 characteristic of geological clay formation. Applied Geochemistry, 124, 104844.
797 https://doi.org/10.1016/j.apgeochem.2020.104844
798 Marignac, C., and Cuney, M. 1999. Ore deposits of the French Massif Central: Insight into the
799 metallogenesis of the Variscan collision belt. Mineralium Deposita, 34(5–6), 472–504.
800 https://doi.org/10.1007/s001260050216
801 Mikulski, S. Z., Williams, I. S., Stein, H. J., & Wierchowiec, J. 2020. Zircon U-Pb Dating of
802 Magmatism and Mineralizing Hydrothermal Activity in the Variscan Karkonosze Massif
803 and Its Eastern Metamorphic Cover (SW Poland). Minerals, 10(9), 787.
804 https://doi.org/10.3390/min10090787
805 Oliver, N. H., McLellan, J. G., Hobbs, B. E., Cleverley, J. S., Ord, A., and Feltrin, L. 2006.
806 Numerical models of extensional deformation, heat transfer, and fluid flows across

basement-cover interfaces during basin-related mineralization. Economic Geology, 101, 1-31.

Ouddou, D. 1984. Le massif de Guerande-le Croisic (Loire Atlantique): Caractérisation géochimique et minéralogique de l'évolution magmatique: Comportement de l'uranium et du thorium.

Ouddou, D., 1984. Le Massif de Guérande-Le Croisic (Loire-Atlantique): Caractérisation géochimique et minéralogique de l'évolution magmatique. Comportement de l'uranium. INPL-CREGU Nancy (Thèse). (309pp.).

Pan, Y., Li, D., Feng, R., Wiens, E., Chen, N., Chernikov, R., Götze, J., & Lin, J. 2021. Uranyl binding mechanism in microcrystalline silicas: A potential missing link for uranium mineralization by direct uranyl co-precipitation and environmental implications. Geochimica et Cosmochimica Acta, 292, 518–531. https://doi.org/10.1016/j.gca.2020.10.017

Parkhurst, D. L., and Appelo, C. A. J. 1999. User's guide to PHREEQC (Version 2): A computer program for speciation, batch-reaction, one-dimensional transport, and inverse geochemical calculations (No. 99-4259). US Geological Survey.

Pearson, F. J., Jr., and Berner, U. 1991. NAGRA thermodynamic database: Core data (Technical Report 91-17). National Cooperative for the Disposal of Radioactive Waste. Villigen, Switzerland: Paul Scherrer Institute.

Polito, P. A., Kyser, T. K., Alexandre, P., Hiatt, E. E., and Stanley, C. R. 2011. Advances in understanding the Kombolgie Subgroup and unconformity-related uranium deposits in the Alligator Rivers Uranium Field and how to explore for them using lithogeochemical principles. Australian Journal of Earth Sciences, 58(5), 453–474. https://doi.org/10.1080/08120099.2011.561873

Post, V. E. A., Vassolo, S. I., Tiberghien, C., Baranyikwa, D., and Miburo, D. 2017. High Uranium Concentrations in Groundwater in Burundi. Procedia Earth and Planetary Science, 17, 524–527. https://doi.org/10.1016/j.proeps.2016.12.132

Poty, B., Leroy, J., Cathelineau, M., Cuney, M., Friedrich, M., Lespinasse, M., and Turpin, L. 1986. Uranium deposits spatially related to granites in the French part of the Hercynian orogen (No. IAEA-TECDOC--361).

Qiu, L., Yan, D.-P., Ren, M., Cao, W., Tang, S.-L., Guo, Q.-Y., Fan, L.-T., Qiu, J., Zhang, Y., and Wang, Y.-W. 2018. The source of uranium within hydrothermal uranium deposits of the Motianling mining district, Guangxi, South China. Ore Geology Reviews, 96, 201–217. https://doi.org/10.1016/j.oregeorev.2018.04.001

Qiu, W., Yang, Y., Song, J., Que, W., Liu, Z., Weng, H., Wu, J., and Wu, J. 2023. What chemical reaction dominates the CO2 and O2 in-situ uranium leaching? Insights from a three-dimensional multicomponent reactive transport model at the field scale. Applied Geochemistry, 148, 105522. https://doi.org/10.1016/j.apgeochem.2022.105522

Qu, H., Liu, H., Tan, K., & Zhang, Q. 2021. Geological Feature Modeling and Reserve Estimation of Uranium Deposits Based on Multiple Interpolation Methods. Processes, 10(1), 67. https://doi.org/10.3390/pr10010067

René, M., and Dolníček, Z. 2017. Uraninite, Coffinite and Brannerite from Shear-Zone Hosted Uranium Deposits of the Bohemian Massif (Central European Variscan Belt). Minerals, 7(4), 50. https://doi.org/10.3390/min7040050

Richard, A., Cathelineau, M., Boiron, M. C., Cuney, M., Mercadier, J., Rozsypal, C., and Pettke, T. 2013. Unconformity-related U deposits: recent advances from fluid inclusions and their host minerals. In 12th SGA Biennial Meeting “Mineral deposits research for a high-tech world” SGA (pp. 1575-1578).

855 Romberger, S. B. (1984). Transport and deposition of uranium in hydrothermal systems at
856 temperatures up to 300 C: geological implications. In Uranium geochemistry, mineralogy,
857 geology, exploration and resources (pp. 12-17). Dordrecht: Springer Netherlands.
858 https://doi.org/10.1007/978-94-009-6060-2_3.
859 Romer, R. L., and Cuney, M. 2018. Phanerozoic uranium mineralization in Variscan Europe –
860 More than 400 Ma of tectonic, supergene, and climate-controlled uranium redistribution.
861 Ore Geology Reviews, 102, 474–504. https://doi.org/10.1016/j.oregeorev.2018.09.013
862 Ruzicka, V. 1993. Vein uranium deposits. Ore Geology Reviews, 8(3–4), 247–276.
863 https://doi.org/10.1016/0169-1368(93)90019-U
864 Ruzicka, V. 1995. Unconformity-Associated Uranium NCONFORMITY-ASSOCIATED
865 URANIUM. https://doi.org/10.1130/DNAG-GNA-P1.197
866 Shen, Jiayue, "Numerical Modeling of Controlling Factors for Formation of Unconformity-
867 Related Uranium Deposits in Sedimentary Basins" 2021. Electronic Theses and
868 Dissertations. 8642. https://scholar.uwindsor.ca/etd/8642
869 Souche, A., Dabrowski, M., and Andersen, T. B. 2014. Modeling thermal convection in
870 supradetachment basins: Example from western Norway. Geofluids, 14(1), 58–74.
871 https://doi.org/10.1111/gfl.12042
872 Spycher, N. F., Issarangkun, M., Stewart, B. D., Sevinç Şengör, S., Belding, E., Ginn, T. R.,
873 Peyton, B. M., and Sani, R. K. 2011. Biogenic uraninite precipitation and its reoxidation
874 by iron(III) (hydr)oxides: A reaction modeling approach. Geochimica et Cosmochimica
875 Acta, 75(16), 4426–4440. https://doi.org/10.1016/j.gca.2011.05.008
876 Steefel, C., Depaolo, D., & Lichtner, P. 2005. Reactive transport modeling: An essential tool
877 and a new research approach for the Earth sciences. Earth and Planetary Science Letters,
878 240(3–4), 539–558. https://doi.org/10.1016/j.epsl.2005.09.017

879 Tartèse, R., Boulvais, P., Poujol, M., Gloaguen, E., and Cuney, M. 2013. Uranium Mobilization
880 from the Variscan Questembert Syntectonic Granite During Fluid-Rock Interaction at
881 Depth. Economic Geology, 108(2), 379–386. https://doi.org/10.2113/econgeo.108.2.379
882 Taylor, S. R., and McLennan, S. M. 1985. The continental crust: its composition and evolution.
883 Timofeev, A., Migdisov, A. A., Williams-Jones, A. E., Roback, R., Nelson, A. T., & Xu, H.
884 (2018). Uranium transport in acidic brines under reducing conditions. Nature
885 communications, 9(1), 1469. https://doi.org/10.1038/s41467-018-03564-7.
886 Tripathi, V. S. 1979. Comments on "Uranium solution-mineral equilibria at low temperatures
887 with applications to sedimentary ore deposits". Geochimica et Cosmochimica Acta,
888 43(12), 1989–1990. https://doi.org/10.1016/0016-7037(79)90011-5
889 Wang, Y., and Chi, G. 2023. Coupling of thermal convection and basin-basement fluid mixing
890 is critical for the formation of unconformity-related uranium deposits: Insights from
891 reactive transport modeling. Chemical Geology, 641, 121764.
892 https://doi.org/10.1016/j.chemgeo.2023.121764
893 Weis, P., Driesner, T., Coumou, D., and Geiger, S. 2014. Hydrothermal, multiphase convection
894 of H_2O-NaCl fluids from ambient to magmatic temperatures: A new numerical scheme
895 and benchmarks for code comparison. Geofluids, 14(3), 347–371.
896 https://doi.org/10.1111/gfl.12080
897 White, D. E. 1968. Environments of generation of some base-metal ore deposits. Economic
898 Geology, 63(4), 301–335. https://doi.org/10.2113/gsecongeo.63.4.301
899 Willey, J. D., Mullaugh, K. M., Kieber, R. J., Avery, G. B., and Mead, R. N. 2012. Controls
900 on the Redox Potential of Rainwater. Environmental Science &and Technology, 46(24),
901 13103–13111. https://doi.org/10.1021/es302569j

902 Woods, P., Fairclough, M., and Tulsidas, H. (Eds.). 2019. Proceedings of the International
903 Symposium on Uranium Raw Material for the Nuclear Fuel Cycle: Exploration, Mining,
904 Production, Supply and Demand, Economics and Environmental Issues (URAM 2014).
905 Zhang, H., Zhang, T., and He, Y. 2023. Reactive transport model of uranium by CO2 + O2 in
906 situ leaching. Environmental Science and Pollution Research, 30(24), 65976–65989.
907 https://doi.org/10.1007/s11356-023-27200-0
908 Zhang, R., Lehmann, B., Seltmann, R., Sun, W., and Li, C. 2017. Cassiterite U-Pb
909 geochronology constrains magmatic-hydrothermal evolution in complex evolved granite
910 systems: The classic Erzgebirge tin province (Saxony and Bohemia). Geology, 45(12),
911 1095–1098. https://doi.org/10.1130/G39634.1
912

Highlights :

- Developed a thermo-hydro-chemical (TH-C) model to investigate uranium mobility in granite-related mineralization within detachment zones.
- Found that uranium can dissolve under reducing conditions with U(IV) as the predominant aqueous species.
- Identified temperature, pH, pe, and an optimal fluid/rock ratio around 1 as critical factors for efficient uranium leaching and precipitation.
- Applied the TH-C model to the Variscan South Armorican Domain, enhancing understanding of uranium mineralization and suggesting applicability to other deposits formed below 300°C.

Declaration of interests

☐ The authors declare that they have no known competing financial interests or personal relationships that could have appeared to influence the work reported in this paper.

☒ The authors declare the following financial interests/personal relationships which may be considered as potential competing interests:

Khaled BOCK reports financial support was provided by CNRS. If there are other authors, they declare that they have no known competing financial interests or personal relationships that could have appeared to influence the work reported in this paper.